

# Advanced Method for Electrical Characterization of Carrier-Selective Passivating Contacts using Transfer-Length-Method Measurements under Variable Illumination

L.-L. Senaud<sup>1,2\*</sup>, P. Procel<sup>3,4</sup>, G. Christmann<sup>1</sup>, A. Descoedres<sup>1</sup>, J. Geissbühler<sup>1</sup>, C. Allebé<sup>1</sup>, N. Badel<sup>1</sup>, P. Wyss<sup>1</sup>, M. Boccard<sup>2</sup>, O. Isabella<sup>3</sup>, M. Zeman<sup>3</sup>, S. Nicolay<sup>1</sup>, M. Despeisse<sup>1</sup>, C. Ballif<sup>1,2</sup> and B. Paviet-Salomon<sup>1</sup>

<sup>1</sup>CSEM PV-Center, Rue Jaquet-Droz 1, CH-2002 Neuchâtel, Switzerland

<sup>2</sup>EPFL, Photovoltaics and Thin Film Electronics Laboratory, Rue de la Maladière 71b, CH-2000 Neuchâtel, Switzerland

<sup>3</sup>Delft University of Technology (TU Delft), Mekelweg 5, 2628 CD Delft, Netherlands

<sup>4</sup>Instituto de Micro y Nanoelectrónica - Universidad San Francisco de Quito, Diego de Robles s/n, Quito 170901, Ecuador

\*corresponding author: laurie-lou.senaud@csem.ch, Tel. +41 32 720 51 29

**Abstract** — Carrier-selective passivating contacts have been demonstrated to be crucial to reach the practical efficiency limit of single junction, crystalline silicon (c-Si) based solar cells. Yet, the electrical transport losses affecting the collection of photogenerated carriers remain to be addressed. To this aim, different methodologies and characterization techniques are currently used. In this contribution, we propose the concept of shell as a new terminology to describe carrier-selective passivating contacts. Then we present a novel characterization methodology using transfer length method (TLM) measurement under variable illuminations to investigate the charge-carrier transport in amorphous/crystalline silicon heterojunction (SHJ) n-type contact stacks. We use TCAD simulation to model a TLM structure and to identify the physical phenomena and the key parameters affecting the contact resistivity ( $\rho_c$ ) and the charge carrier accumulation of such contact stacks. Then, the simulation results are compared to experimental data by performing variable-illumination TLM measurements of actual SHJ n-type contact stacks. Specifically, we demonstrate that illumination has a strong impact on the measured  $\rho_c$  value, highlighting the importance of measuring  $\rho_c$  under maximum power point conditions for a relevant characterization of solar cell transport losses. In addition, we investigate the dependence of the  $\rho_c$  to a change in the injected carrier density within the c-Si bulk to compare the illumination response of different SHJ n-type contact stack. In the quest for maximal efficiency, this method may insightfully complete other characterization techniques to further understand and study the electrical transport in solar cells.

**Index Terms** — Passivating contacts, shell, electrical losses, transport, contact resistivity, transfer length method, illumination, injection levels, maximum power point condition, silicon heterojunction.

## I. INTRODUCTION

The use of carrier-selective passivating contacts has been theoretically identified [1] and experimentally demonstrated [2], [3] to be the most promising way to reach the practical efficiency limit of single junction, crystalline silicon (c-Si) based solar cells. One way to overcome the remaining efficiency losses is to mitigate the transport losses affecting the extraction of photogenerated carriers [4] by improving the passivation quality and by reducing the resistive losses, both resulting in an improvement in the overall selectivity of the so-called *contacts* of solar cells [5]. Along these lines, this paper is split in two main parts. In the first one, we present a generalized and unambiguous description of contacts in solar cells by introducing the terminology of *shell* [6]. This aims to accurately investigate – and eventually mitigate – the electrical as well as the optical losses affecting state-of-the-art solar cells. Importantly, this terminology enables to go beyond the limitations of the term of *contacts*, which is indifferently used to refer to any part of the solar cell where

the generated carriers are extracted, and therefore to precisely consider the interfaces and the physical properties coupling present between the different material layers in solar cells. In a second part, we present a novel characterization method based on an upgraded theoretical framework of transfer length method (TLM) measurements. To characterize the resistive losses of contact stacks, the TLM measurement has been widely used to determine their contact resistivity ( $\rho_c$ ) and thus to quantify their electrical losses once integrated in solar cells. Currently however,  $\rho_c$  measurements are performed in dark condition and thus do not consider the impact of the injection present inside the c-Si bulk on electrical transport quality. In this work, we use TLM measurements under variable illumination to further study specific shells including different electron-collecting contact stacks in the amorphous/crystalline silicon heterojunction (SHJ) technology [7]. Using this improved characterization method we demonstrate (i) that illumination, and thus the injected carrier density inside the c-Si bulk, has a strong impact on the  $\rho_c$  value, (ii) the importance of measuring  $\rho_c$  under maximum power point (MPP) conditions for a relevant characterization of solar cell transport losses and (iii) how the dependence of the  $\rho_c$  to a change in the injected carrier density within the c-Si bulk provides additional insight to compare the illumination response of different SHJ n-type contact stacks. To complete our experimental results, Technology Computer-Aided Design (TCAD) simulations are used to model the TLM structure and to identify the physical phenomena and the key parameters affecting the  $\rho_c$  and the selectivity of several SHJ n-type contact stacks. In addition, the suspected limitations and physical phenomena appearing during such TLM measurements are elucidated. Overall, this work provides additional important insights into the fundamental understanding and the practical characterization of SHJ solar cells, as well as useful methods to guide the actual efficiency improvement of such devices towards their practical efficiency limits.

## II. METHOD

### A. Shell of Solar Cells

#### 1) General frame

In an approach proposed by [1], a solar cell can be seen as a balloon inflated with light-generated carriers. This “balloon” corresponds to the solar cell absorber where electron-hole pairs are generated by converting the energy of the incoming light. In general, to efficiently extract these photo-generated carriers out of the absorber bulk, three electrical functions must be fulfilled, namely (i) passivation, to avoid recombination at the surface of the absorber, (ii) selectivity, to spatially separate the holes and the electrons at different absorber locations, and (iii) terminal electrodes to extract the carriers outside the absorber and to inject them into an external load. Previously, the term *membrane* was introduced by [8] to describe materials providing selectivity, and similarly the term *skin* was proposed by [1], [9] to describe passivation in addition to selectivity. Recently, following the pioneering work of Yablonovitch [10], the ability to provide selectivity in addition to passivation has been defined as a *carrier-selective passivating contact* (CSPC), i.e. a contact which passivates the surface of the absorber, and which blocks one type of carriers to escape from the absorber while allowing the other one to be extracted. Prime examples of CSPC are the SHJ technology [7], as well as various approaches based on a thin tunnelling oxide capped with polycrystalline silicon, such as the TopCON [11] and the POLO [12] concepts. However, in these cases, the term *contact* is ambiguous as it can also equally refer to many different sub-elements constituting it [13]. Indeed, all so-called *contact* schemes for solar cells actually consist in several stacked materials and/or material with locally changing properties, thus creating various interfaces and *contacts* between those. This section therefore aims at providing a generalized and unambiguous description of contacts in solar cells, allowing to accurately investigate – and eventually mitigate – the electrical as well as the optical losses affecting state-of-the-art solar cells: the terminology of *shell* [6].

As defined in the frame of this work, the shell must fulfil the three above-mentioned electrical functions required for efficient carrier extraction, i.e., passivation, selectivity, as well as providing terminal electrodes. In addition, the shell must comply with optical requirements so as not to hinder the light absorption in the absorber. More specifically, at the front side of solar cells, the shell must be highly transparent to minimize the parasitic absorption losses. At the rear side, depending on the solar cell architecture, the shell might be required to be highly transparent as well (e.g., to ensure

a high bifaciality), and to provide in addition a high internal reflection to increase the photons optical path in the absorber bulk. As a result, the most important challenge of a shell is to fulfil all these electrical and optical functions altogether with as few losses as possible, to reach high quality light collection and carrier extraction, thus eventually allowing high conversion efficiency. Depending on the solar cell technology, the shell may consist in a unique material with locally changing properties, and/or in a stack of several thin layers made from different materials. The doping gradient in the silicon absorber used in the Al-BSF technology is a typical example of the former case, whereas the intrinsic and doped hydrogenated amorphous silicon, transparent conductive oxide (TCO), and metal layer stacks in the SHJ technology is a perfect example of the latter. Generalizing, it means that the shell includes all the parts of the solar cell located at both sides of the absorber between the near-surface modified region of this latter to the last terminal electrodes included, before the external load. Importantly, the global shell characteristics and its ability to provide the three required electrical functions, as well as the optical ones, are defined by the global coupling of all the components constituting it. In the case of electrical properties, this coupling is evidenced by the energy band-bending occurring when the different elements constituting the shell are brought together. Note that due to this coupling, the “influence” of the shell might also extend into a part of the absorber bulk close to its surface, such as a space charge region (SCR) induced via the energy band-bending. This is depicted in Figure 1a and Figure 1b.

As briefly mentioned above, in the specific case of the SHJ technology, the shell is composed by a stack of several thin layers made out of different materials. These are intrinsic hydrogenated amorphous silicon (a-Si:H(i)), doped hydrogenated silicon layers, TCO, and metal layers, deposited on both side of the n-type silicon bulk (c-Si(n)). Such a shell in the case of a two side-contacted solar cell is illustrated in Figure 1a<sup>[1]</sup>. In this case, it appears clearly that the shell is composed by several interfaces and sub-contacts defined by the coupling of the different thin layers and the silicon bulk. The latter are highlighted as orange-hatched areas in Figure 1a and Figure 1b. The coupling of the physical properties of the different materials, including the c-Si(n) bulk, defines the overall energy-bands bending presented in the space domain in Figure 1b and shapes the global electrical properties. Thus, due to this coupling, the addition, removal or change of a single shell sub-component or of the c-Si(n) bulk directly affects the global energy-band arrangement, this latter being difficult to predict precisely *a priori*. Each shell layer must then be developed considering its resulting coupling with all other sub-components and the silicon bulk. It is thus challenging to optimize only one part of the SHJ shell without affecting the resulting electrical properties. Closing this comprehension gap requires to take a closer look at the way the photo-generated carriers move within the energy-band structure; this is the topic of section II.A.2) below.

Figure 1. (a) Sketch of a SHJ shell in the case of a typical two side-contacted solar cell. The c-Si bulk coupled with the two parts of the shell (encompassing the different material layers) are represented. These are the intrinsic amorphous layer (i), p and n-type thin silicon layers ((p) and (n), respectively), as well as TCO and metal layers. All these sub-layers coupled together define the three different electrical functions (passivation, selectivity and terminal electrode) which are partly revealed in the energy-band diagram in (b). The several interfaces and sub-contacts defined by the different sub-layers are represented in orange-hatched areas. Finally, the CSPC range effect extending from the TCO to inside the c-Si bulk is also represented in light-orange dashed areas. (b) Corresponding schematic energy-band diagram in the space domain for open-circuit condition and under injection. The conduction and the valence bands energies ( $E_c$  and  $E_v$ , respectively), as well as the band-bending (spatial evolution of the energy states) are represented spatially for the different SHJ materials layers. The electron and hole quasi-Fermi levels ( $E_{F_n}$  and  $E_{F_p}$  respectively) are also depicted spatially through the c-Si(n) bulk and the shell. The conduction and the valence band offsets with their respective energies ( $\Delta E_c$  and  $\Delta E_v$ , respectively) are also depicted. The latter build different energy barriers affecting the transport of the generated carriers.

<sup>[1]</sup> Note that in back-contacted solar cells, the purposes of the front part of the shell are passivation and optical losses minimization only, since the carrier-selective and electrode aspects are performed by the rear part of the shell in addition to passivation.

## 2) Carrier Transport, Contact Resistivity and Selectivity

*Transport* is defined in this work as every single displacement of photo-generated carriers, expressed by the change in carrier concentration along position and time (continuity equation), from their generation location until their extraction at the terminal electrodes of the shell. The transport is thus the flow of both carrier types from the absorber through the shell, in their way to their selective areas and final respective electrodes. The quality of the carrier transport is impacted by two physical phenomena, namely recombination and resistive effects, both resulting in electrical losses. Recombination is the result of a loss of carriers which induces a chemical potential drop; its magnitude is defined by the absorber bulk quality and the shell passivation ability. In contrast, resistive effects are the result of drift-diffusion and interface's phenomena which induce an electrical potential drop when both carrier types flow from their generation location inside the absorber to the terminal electrodes, passing through the shell. Both electrical losses impact the final device performances, with the pseudo-voltage ( $pV$ ) reflecting the recombination losses, and the series resistance ( $R_S$ ) reflecting the resistive losses [1], [8]. To reach high fill factor (FF), and eventually high conversion efficiency,  $pV$  must be maximized while  $R_S$  must be minimized. Nowadays, in state-of-the-art, single junction, crystalline silicon (c-Si) based solar cells, the contribution of the c-Si bulk to the remaining electrical losses is no more limiting the solar cell performances, as it operates close to its Auger limit and features a suitable conductivity [14]. Rather, the main contributions to the remaining electrical losses are dictated by the shell itself, therefore best-in-class c-Si solar cells are nowadays *shell-limited* devices [15], [16]. It turns out from this electrical transport analysis that improving the c-Si solar cells conversion efficiency requires to mitigate the recombination losses and the resistive effects incurred by the shell. To do so, the shell must enable a large quasi-Fermi levels splitting inside the bulk in addition to a minimal chemical drop until the terminal electrodes, together with providing minimal supplemental resistive effects in addition to the absorber own resistance.

As already mentioned in section II.A.1), SHJ shells aim at meeting these requirements by combining thin layers of different materials. However, this layer combination induces several energy barriers stemming from discontinuities in the energy-band structure, arising at the hetero-interfaces created between the different materials constituting the SHJ shell, leading to resistive losses [17]. Such energy barriers are clearly visible in the energy-band diagram of the SHJ shell sketched in Figure 1b, e.g., at the interface between the c-Si(n) bulk and the intrinsic amorphous silicon layers as well as between the doped thin silicon layers and the TCO. The overall energy-band bending and alignment, including the energy barriers characteristics (such as their height and width), is governed by the coupling of the physical properties of the different materials constituting the shell as well as by the c-Si(n) bulk properties. In particular, the band bending is defined by the Fermi-energy among the device, from c-Si bulk to TCO. More precisely, the Fermi and quasi-Fermi levels are determined by the c-Si absorber carrier density, the thickness, the activation energy ( $E_a$ ), and the defect density of the thin silicon layers, as well as the work function (WF) and the carrier concentration ( $N_{TCO}$ ) of the TCO layer, among others [4], [18]. These physical parameters define the energy position of the conduction and the valence bands with respect to the Fermi level for the c-Si wafer and for each material layer. Carrier transport through the hetero-interfaces located along the energy-band diagram occurs by two different general mechanisms, namely thermionic emission and tunnelling. In the specific case of SHJ shells, several tunnelling processes have been identified [19] and thoroughly described, these are: direct tunnelling (DT) [20], band-to-band tunnelling (B2BT) [21] and trap-assisted tunnelling (TAT) [22]. These processes are thus connected to the band-bending at the c-Si/a-Si:H(i), a-Si:H(i)/doped thin silicon layer and doped thin silicon layer/TCO interfaces. Eventually, when all these effects result in an ohmic current-voltage (I-V) behaviour under relevant operating conditions, the corresponding resistive electrical transport losses affecting carrier extraction can be accounted by a contact resistivity value ( $\rho_c$ ). In that case, this parameter allows one to assess the global carrier transport quality through all the hetero-interfaces and the materials composing SHJ shells. Any change to the energy barriers or to the bulk properties of the materials constituting the shell and of the c-Si bulk will directly affect the  $\rho_c$  value [17]. The parameter  $\rho_c$  reflects then the effect on transport of the global band-bending resulting from the properties coupling of the different materials and is therefore a relevant parameter to investigate different interfaces within and induced by the shell.

More specifically, at the vicinity of the c-Si/a-Si:H(i) interface, a change of the c-Si bulk injected carrier density, i.e., a quasi-Fermi level change inside the c-Si bulk, will affect the local band-bending inside the c-Si bulk and thus affect the accumulation of carriers at this location, potentially impacting the  $\rho_c$  value. Said differently, the value of  $\rho_c$  is expected to depend strongly on the injection conditions. On another hand, the energy band-bending also rules the selectivity of a given shell. Indeed, in the case of SHJ, selectivity is ruled by the ratio between the conductivities of majority and minority charge carriers inside the absorber at the vicinity of the c-Si/a-Si:H(i) interface [5]. Yet, as electron and hole mobilities are of the same order of magnitude inside c-Si [23], [24], a high selectivity requires a high asymmetry in carrier concentration close to this interface. In the case of SHJ, this asymmetry results in carrier accumulation inside the c-Si bulk close to the c-Si/a-Si:H(i) interface, such as the higher the accumulation the higher the selectivity [25], [26]. To enforce different accumulation conditions, the activation energy of the thin silicon layers was proven to be a relevant parameter. This parameter is equal to the energy difference between the Fermi level and the current transporting band, i.e., the conduction band for the case of electrons and the valence band for the case of holes. Thus, the lower the  $E_a$ , the higher the doping of the thin silicon layer. As demonstrated in [4], a low (respectively high)  $E_a$  was found to allow for a high (respectively low) selectivity owing to a high (respectively low) accumulation close to the c-Si/a-Si:H(i) interface. Consequently, for SHJ shells, the  $\rho_c$  and selectivity are expected to depend on the injection condition, for instance induced by variable illumination: this forms the rationale of our investigation.

### B. TLM Sample Fabrication and Measurement

TLM samples were fabricated on 240- $\mu\text{m}$ -thick, float-zone n-type c-Si wafers (c-Si(n)) with a resistivity of 2.8  $\Omega\cdot\text{cm}$ . The wafers were textured on both sides in an alkaline solution to create random pyramids and then wet chemically cleaned. Before the deposition of the required layers, the native silicon oxide was removed in a diluted hydrofluoric solution. Thin blanket of a-Si:H(i) films were afterwards deposited on both sides of the wafer for surface passivation by plasma-enhanced chemical vapour deposition (PECVD), using an Indetec Octopus II system. Then, a thin blanket p-type a-Si:H film (a-Si:H(p)) was immediately deposited, with the same deposition system, at the TLM samples rear side. On the front side of the TLM samples, different n-type thin silicon multilayers combining a thin bottom amorphous buffer layer and different top nanocrystalline layers (referred to as a-Si:H(n)/nc-Si:H(n)) were deposited to reach different  $E_a$  (see Table 1). The thin bottom buffer a-Si:H(n) layer is kept the same for all multilayers. More details on our thin silicon layer stacks can be found elsewhere [27]–[30]. An indium tin oxide (ITO) layer was afterwards deposited at the rear side of the TLM samples, on the top of the a-Si:H(p) layer, using DC magnetron sputtering with an  $\text{In}_2\text{O}_3\text{:SnO}_2$  (ITO) target. The thickness of this rear ITO layer measured on planar bare glass substrate was 110 nm, which leads to an optimal thickness for anti-reflective coating (ARC) on textured wafer. The combination of a-Si:H(i)/a-Si:H(p)/ITO at the rear side of the TLM samples allows then to reach a good passivation quality together with an optimized ARC, and thus to maximize the injected carrier concentration reached in the c-Si(n) bulk of the TLM samples for a given illumination. Note that the presence of the a-Si:H(p) layer prevents any electron current to go through the ITO rear layer, hence restricting it to the c-Si(n) bulk. At the front side of TLM samples, aluminium-doped zinc oxide (AZO) was deposited by RF magnetron sputtering with an Oerlikon Clusterline tool, on the different n-type thin silicon multilayers. This AZO layer features a carrier concentration of  $1.5 \times 10^{20} \text{ cm}^{-3}$  and a thickness of 180 nm on glass substrate. The different shells manufactured as presented above and used for this study are listed in Table 1. The shells #1 to #4 feature similar high passivation quality at the rear side but different n-type multilayers at the front side with thickness from 34 to 89 nm along with  $E_a$  from 17 to 265 meV. The shell #5 features the same n-type multilayers than shell #1 but a low rear side passivation quality.

Table 1. List of the different shells under study with the thickness and activation energy of the a-Si:H(n)/nc-Si:H(n) as well as the quality of the rear side passivation. The rear passivation quality is tuned with the a-Si:H(i)/a-Si:H(p) stack. The back ITO, the front AZO and Ag are the same for all shells.

n-type multilayer			
Shell	$E_a$ (meV)	Thickness (nm)	Rear side passivation quality
#1	265	39	High
#2	173	34	High
#3	48	37	High
#4	17	89	High
#5	173	34	Low

The thicknesses of the n-type multilayers were measured on planar glass substrates using reactive ion etching to create a thickness step, its height being measured using a stylus profilometer. Their activation energy was measured by temperature-dependent dark conductivity measurement [31]. The TCO thicknesses were assessed by a stylus profilometer and their carrier concentration ( $N_{TCO}$ ) was measured by Hall effect measurement in the Van der Pauw configuration [32], in both cases on bare planar glass witness samples. Finally, a 400-nm-thick silver (Ag) rear blanket layer was sputtered over the whole AZO layer. After this step, TLM samples were annealed at 210 °C for 30 minutes. It is important to note that thanks to our large-area PECVD and PVD tools, within a single experiment, all TLM samples were co-deposited with identical a-Si:H(i), a-Si:H(p), ITO and rear blanket Ag layers. Therefore, only each specific n-type thin silicon multilayers and AZO depositions were performed individually for each TLM sample. Then, TLM patterns featuring a length (L) of 2 mm as well as gaps of 0.5, 1.0, 1.5, 2.0, 2.5 and 3.0 mm were printed using a protective ink mask. The Ag and AZO layers were then etched between the pads, and the ink was removed. After these etching steps, the TLM samples were cut with a selected width (w) of 6 mm to create edge isolation. This isolation is needed to confine the current flow and to avoid additional errors caused by edge effects, i.e. to prevent the current flowing away from the edges of the TLM pads before being recollected. To do this, the TLM samples were first pre-cleaved at the rear side using a laser and then cut manually. Then, the interpad distances were precisely measured thanks to a microscope, as they may slightly differ from their nominal value. A sketch of our typical TLM sample and design is given in Figure 2. I-V measurements were performed on each completed TLM sample in dark condition and under different illuminations using a Wacom class AAA light simulator and different filters to reach injected electron density ( $\Delta N_e$ ) up to about  $5.96 \times 10^{15} \text{ cm}^{-3}$ , defining the 100% illumination level. The TLM samples were illuminated from the a-Si:H(i)/a-Si:H(p)/ITO side using a flip table to ensure a homogenous injection below and between each TLM pad. From these I-V curves, the TLM computation was performed and the output parameters, namely the contact resistivity ( $\rho_c$ ), contact resistance ( $R_c$ ), sheet resistance ( $R_{sh}$ ) and transfer length ( $L_T$ ) were extracted. Finally, corrections on the value of  $\rho_c$  considering the wafer thickness of the TLM samples were performed for each illumination as presented in [33]. Finally, for each illumination, the  $\Delta N_e$  values were calculated from the wafer  $R_{sh}$ , taking into account the dependence of the electron mobility on the injection [23].

Figure 2. Cross-section of the experimental samples (left) and top view showing the TLM pads layout (right).

### C. Finite Element Simulations for TLM

To model the TLM structure and to simulate the value of  $\rho_c$  as a function of the c-Si(n) bulk injected carrier density, opto-electrical simulations were performed using TCAD Sentaurus [34]. This simulation platform rigorously solves the drift-diffusion equations together with interface physics (tunnelling, thermionic emission, recombination, etc). This allows to consistently assess the transport mechanisms through the hetero-interfaces of the shells under study. The simulated TLM structure consists in two identical contact pads on top of a c-Si(n) bulk spaced by variable gaps as used on actual sample (0.5, 1.0, 1.5, 2.0, 2.5 and 3.0 mm). Each contact width is 1.0 mm and the n-type contact stack is

formed by 6 nm of a-Si:H(i), 30 nm of n-type thin silicon layer and 180 nm of TCO. The c-Si(n) bulk features a wafer resistivity of  $3 \Omega\cdot\text{cm}$  which gives a doping of  $1.55\times 10^{15} \text{ cm}^{-3}$ . The  $E_a$  values were adjusted by a uniform doping concentration in a defective background of doped layers to achieve 17, 48, 173 and 265 meV (similar to the experimental values presented in Table 1). The TCO was modelled as a degenerate semiconductor [4], [35], thus work-function mismatches and induced band bending are accurately considered. The TCO carrier concentration ( $N_{\text{TCO}}$ ) was set to  $1.44\times 10^{20} \text{ cm}^{-3}$ . Further details on the TLM modelling can be found in [4], [17], [36]. To change the injected carrier density inside the c-Si bulk for a given shell, different injection levels, and thus different electron quasi-Fermi level ( $E_{\text{Fn}}$ ), are emulated inside the c-Si bulk absorber using different carrier generation rates equivalent to the targeted light intensities. A reference optical generation profile was adjusted based on ray-tracing optical simulations to reach  $39 \text{ mA/cm}^2$ , which is a typical current density in solar cells using SHJ shells. This generation profile was fixed to be the 100% of illumination and accordingly, TLM structures were evaluated in dark, 7, 13, 50 and 100% illumination by scaling the generation rate. The recombination rate inside the c-Si bulk ( $\tau_{\text{bulk}}$ ) was adjusted to reach a  $\Delta N_e$  of about  $4.85\times 10^{15} \text{ cm}^{-3}$  for the 100% illumination. The corresponding energy-band diagrams for these different illuminations were simulated and considered. From the latter, the SCR widths ( $w_{\text{SCR}}$ ) inside the c-Si(n) bulk was calculated considering its extent from the first decreasing point of the energy conduction band ( $E_c$ ) to the c-Si(n)/a-Si:H(i) interface location. The conduction band energy height ( $E_h$ ) was also calculated considering the energy difference between the flat part of the  $E_c$  and the minimum energy at c-Si(n)/a-Si:H(i) interface. Finally, the electron and hole accumulations were calculated performing the ratio of the electron (resp. hole) density at c-Si(n)/a-Si:H(i) interface to the electron (resp. hole) density inside the bulk. These parameters were calculated for the different illuminations and  $E_a$  under study. Then, each TLM structure was simulated to obtain the current vs. voltage response from -1 to 1 V and the TLM methodology was applied to extract  $R_{\text{sh}}$  and  $\rho_c$ .

#### D. Edges Recombination Impact on Contact Resistivity Measurement

As described in section II.A.2), the TLM samples under investigation have cut edges to create current isolation. Their edges are consequently unpassivated and important recombination losses occur there. Under illumination, this induces a non-homogeneous excess carrier concentration from the middle of the TLM pad width ( $w$ ) to its edges, and thus leads to a corresponding c-Si(n) wafer resistivity variation. The latter is expected to be lower at the centre of the pads than at the edges. Consequently, the  $R_{\text{sh}}$  of the c-Si(n) TLM conductive layer is non-homogeneous and varies along the  $w$  direction. This again breaks one of the fundamental hypotheses of TLM which assumes homogeneous  $R_{\text{sh}}$  to ensure an evenly distributed current flow between two pads. *A priori*, there is no simple way to rigorously extract the contact resistivity in such case. However, it is possible to evaluate its impact on the  $\rho_c$  value extracted with the standard TLM approach. To do this, the one-dimensional drift-diffusion solver PC1D [37] was used to simulate an inhomogeneous excess carrier concentration profile inside a 1D structure, allowing to consider one direction corresponding to the direction parallel to  $w$  in real samples. The material of the 1D structure is defined as a c-Si(n) bulk with a doping of  $1.7\times 10^{15} \text{ cm}^{-3}$ , which is close to the value measured on experimental samples. Its length was set to 6 mm corresponding to the width of actual TLM samples. The interface recombination velocities for electron ( $S_n$ ) and holes ( $S_p$ ) at both edges were assumed to be equal to  $S_n = S_p = 10^7 \text{ cm/s}$ , which corresponds to the highest thermal velocity of carrier transport and is large enough to consider that all excess carriers have recombined at the edges. The simulated 1D structure used is depicted in Figure 3 and compared to an actual TLM sample. To simulate the different illuminations under study, several generation profiles were defined. Each of them is established to be homogeneous for each position inside the simulated structure in order to reproduce the experimental generation of TLM sample. The latter being illuminated from the back side, the generation is then homogeneous along the  $w$  direction. The 1 sun generation profile was set to an average constant generation of  $9.68\times 10^{18} \text{ cm}^{-3}\text{s}^{-1}$ . This generation corresponds to the typical value presents inside SHJ solar cells using similar thin silicon layers, TCO and bulk thickness as the actual TLM samples. Finally, the carrier lifetimes defined experimentally by bulk and shell passivation quality are simulated in PC1D using the single Shockley-Read-Hall lifetime parameters ( $\tau_{\text{SRH}}$ ). Thus, by solving the drift-diffusion equation for this 1D test structure with PC1D, it is possible to simulate the electron density profile ( $N_e(x)$ ) along the 1D direction. This profile

is expected to be representative of what can be observed in an experimental TLM structure, along the pad width direction, assuming negligible transport in the other directions. Thus, considering a TLM c-Si(n) bulk of thickness  $d$ , it is possible to calculate the corresponding electron sheet resistance profile ( $R_{sh}(x)$ ) for any  $x_i$  position below the TLM pad using equations (1) and (2), with  $q$  equal to the elementary charge and an electron mobility ( $\mu_n$ ) of  $1330 \text{ cm}^2\text{V}^{-1}\text{s}^{-1}$  assuming that in the range under study the photogenerated carriers have little impact on mobility [23], [24].

$$\sigma_e(x_i) = q\mu_n N_e(x_i) \quad (1)$$

$$R_{sh}(x_i) = \frac{1}{\sigma_e(x_i) \times d} \quad (2)$$

Here  $x_i$  stands for the  $i$ -th position of the simulation domain mesh. From the  $R_{sh}(x)$  profiles it is then possible to calculate an average value of equivalent  $R_{sh}$  ( $R_{sh_{eq.}}$ ) with equation (3), which is approximated by considering the conduction of parallel resistances between two TLM pads. This approach thus neglects the lateral transport effects in the wafer along the TLM width direction, as was done in [38] for evaluating the impact of silver line resistance on TLM structures, where it was shown to have very little impact.

$$R_{sh_{eq.}} = \frac{1}{\sum \left( \frac{\Delta x_i}{R_{sh}(x_i)} \right)} \times \sum x_i \quad (3)$$

Under injection,  $R_{sh}(x)$  is experimentally driven by bulk and surface recombination of actual TLM samples. In the simulation, all recombination are lumped in one  $\tau_{SRH}$  term, which is then adjusted to get  $R_{sh_{eq.}}$  simulated from PC1D to match the average value of  $R_{sh}$  measured experimentally for each illumination. Then, in the case of a  $\rho_c$  which depends on the excess carrier concentration, as it is the case in this work and will be presented in sections III.A.2) and III.C, a contact resistivity profile ( $\rho_c(x)$ ) induced by  $R_{sh}(x)$  is present below the TLM pad width. From  $\rho_c(x)$  it is possible to calculate the transfer length profile ( $L_T(x)$ ) and contact resistance profile ( $R_c(x)$ ) present below a pad using the TLM equations (equation (4) and (5)) with  $L = 2 \text{ mm}$  the TLM pad length.

$$L_T(x_i) = \sqrt{\frac{\rho_c(x_i)}{R_{sh}(x_i)}} \quad (4)$$

$$R_c(x_i) = \frac{\rho_c(x_i)}{\Delta x_i L_T(x_i)} \times \coth\left(\frac{L}{L_T(x_i)}\right) \quad (5)$$

Then, knowing  $R_c$  and  $R_{sh}$  for all position  $x_i$  on the  $x$ -mesh, and considering all the resistance in parallel (i.e. neglecting here again lateral transport along the TLM width direction), it is possible to compute the total TLM resistance ( $R_{TLM_k}$ ) for each interpad distance  $k$  using equation (6) and (7).

$$\frac{1}{R_{TLM_k}(x_i)} = \frac{1}{2R_c(x_i) + R_{sh}(x_i) \times \frac{gap_k}{\Delta x_i}} \quad (6)$$



$$R_{TLM_k} = \frac{1}{\sum \left( \frac{1}{R_{TLM_k}(x_i)} \right)} \quad (7)$$

Finally, from the plot of  $R_{TLM_k}$  as a function of the interpad distance  $k$  it is possible to perform TLM computation and to get the values of  $R_{sh_{eq}}$ ,  $R_c$ ,  $L_T$  and thus  $\rho_c$ . These output parameters which are obtained considering an inhomogeneous  $R_{sh}(x)$  profile are then compared to the ones obtained experimentally using the standard TLM computation which consider homogeneous  $R_{sh}$ , i.e. neglecting the  $R_{sh}$  inhomogeneity due to edge recombination.

Figure 3. Schematic description of the PC1D structure for simulating the recombination effects at the TLM samples edges.

### III. RESULTS AND DISCUSSION

#### A. Finite Element Simulations for TLM measurements

##### 1) Illumination and Non-ohmic Behaviour

During our investigation, one of the first observed phenomena was the presence of non-ohmic TLM I-V curves with the augmentation of the illumination. This phenomenon was thoroughly investigated as it was first thought to be a limitation to perform TLM computation. Indeed, a non-ohmic behaviour would break the fundamental TLM hypothesis requesting the ohmicity of the shell part under investigation. Figure 4a shows the simulated I-V curves obtained between two TLM pads as a function of the illumination for a shell with  $\tau_{bulk}$  of 0.4 ms. It is observed that a non-ohmic behaviour appears above a certain illumination threshold, here 13 %. This non-ohmic behaviour becomes stronger as the illumination increases and is independent of the different  $E_a$  under study (data not shown). Additionally, Figure 4b plots the simulated I-V curves between two TLM pads under 13 % illumination for different  $\tau_{bulk}$ . In this case, it is observed that the non-ohmic behaviour becomes increasingly noticeable upon the rise of  $\tau_{bulk}$ , again regardless of the  $E_a$  value (data not shown). In both cases presented in Figure 4a and Figure 4b, increasing the illumination or the  $\tau_{bulk}$  results in an augmentation of the generated carrier concentration inside the c-Si bulk. Thus, the trigger of the non-ohmic behaviour is revealed to be the quantity of injected carriers inside the c-Si(n) bulk, rather than the illumination level or the recombination mechanisms alone. This non-ohmic behavior is therefore proven not to stem from an effect of the shell properties but from the c-Si bulk properties. The experimental evidences as well as the physical origin of the non-ohmic behaviour and how to accurately extract the value of  $\rho_c$  in these conditions are presented in section III.B.1) and III.B.2).

Figure 4. Simulated I-V curves between two TLM pads as a function of the illumination for a  $\tau_{bulk}$  fixed to 0.4 ms (a) and as a function of the bulk lifetime for an illumination fixed to 13 % (b).

##### 2) Illumination and impact on $\rho_c$

Figures 5-8 show the impact of changing  $E_a$  of the n-type thin silicon layer (17, 48, 173 and 265 meV) and of varying the illumination on: the conduction band energy in the space domain (Figure 5), the two band parameters  $w_{SCR}$  and  $E_h$  (Figure 6), the electron and hole accumulations (Figure 7), and the ratio of electron to hole at the c-Si(n)/a-Si:H(i) interface (Figure 8). On the first hand, it is observed that as expected, in the dark, the electron accumulation is more pronounced for low  $E_a$  compared to high  $E_a$ . Upon increasing  $E_a$  from 17 meV to 265 meV,  $w_{SCR}$  decreases from 820 to 725 nm and  $E_h$  decreases from 0.22 to 0.13 eV (see Figure 6), resulting in an electron accumulation reduction from  $2.91 \times 10^3$  to  $8.86 \times 10^1$  (see Figure 7a). In contrast, the hole accumulation is found to be higher for high  $E_a$  compared to low  $E_a$ , increasing from  $3.25 \times 10^{-4}$  to  $1.13 \times 10^{-2}$  (see Figure 7b). Finally, looking at the ratio of electron to hole at the c-Si(n)/a-Si:H(i) interface, it is observed that the latter is higher for lower  $E_a$  (see Figure 8). Overall, this highlights that a higher electron accumulation and thus a higher electron-selectivity in the dark is obtained for lower  $E_a$ , as discussed in section II.A.2). Then, looking at the different illuminations, we observe that for all  $E_a$  considered here, the conduction band and the quasi-Fermi level are getting closer, resulting in an electron density augmentation (see Figure 5) and

affecting the band parameters: indeed,  $E_h$  and  $w_{SCR}$  decrease upon increasing illumination (see Figure 6). This will directly affect the electron accumulation which is found to reduce with illumination increase (Figure 7a). In addition, by rising the illumination, the hole density rises as well, impacting the hole accumulation which is found to increase upon illumination for all the different  $E_a$  under investigation (see Figure 7b). In particular, the ratio of electron to hole at the c-Si(n)/a-Si:H(i) interface reduces with the illumination increase, demonstrating that the electron selectivity is therefore impacted by illumination such as the higher the illumination, the lower the electron selectivity (Figure 8). Overall, Figures 5-7 show that the decrease of the value of these parameters is independent from  $E_a$  but is only dependent on the illumination. In addition, when the illumination varies, the electron (resp. the hole) accumulation for low  $E_a$  stays always higher (resp. lower) compared to high  $E_a$ .

Figure 5. Energy-band diagrams illustrating the different  $E_c$  as a function of the illumination for the different n-type thin silicon layers featuring  $E_a$  of 17, 48, 173 and 265 meV. The  $w_{SCR}$  and the  $E_h$  in dark condition, as well as the difference of  $E_h$  between dark and 100% illumination ( $\Delta E_h$ ) are depicted.

Figure 6.  $E_h$  (a) and  $w_{SCR}$  (b) as a function of illumination for the different  $E_a$ .

Figure 7. Electron (a) and hole (b) accumulation as a function of illumination for the different  $E_a$ .

Figure 8. Ratio of electron to hole at c-Si(n)/a-Si:H(i) interface as a function of illumination for the different  $E_a$ .

Figure 9a-d show the  $R_{sh}$  and  $\rho_c$  values extracted from TLM simulations for the different  $E_a$  and the various illuminations. Figure 9a shows that, as expected, the  $R_{sh}$  decreases with rising the illumination; this behaviour directly owes to an augmentation of the electron density ( $N_e$ ) under higher illumination, the latter being the same for the four different  $E_a$  as the passivation quality is similar for the different shells under study. In contrast, Figure 9b shows that  $\rho_c$  drastically increases with illumination for all the investigated  $E_a$ . It is observed that the higher the  $E_a$ , the higher the increase of  $\rho_c$  with illumination. Figure 9c shows  $\rho_c$  as a function of  $R_{sh}$ . Starting from the  $R_{sh}$  value in the dark (hence the bottom right points in the graph), it is observed that for all  $E_a$ ,  $\rho_c$  increases linearly as the  $R_{sh}$  decreases, but with different slopes. These slopes correspond to the response of the n-type contact stacks to the illumination; said differently, the higher the slope, the higher the impact of the illumination, and thus of the injected carrier density on the contact resistivity. The slopes extracted from the  $\rho_c=f(R_{sh})$  linear curves are plotted in Figure 9d. Here, we observe that the higher the  $E_a$ , the higher the slope of the  $\rho_c=f(R_{sh})$  curve and thus the higher the impact of the illumination on the shell under study. This may suggest that a higher electron accumulation, and thus a higher electron selectivity in the dark, will result in a lower slope and thus in a smaller impact of the illumination on the shell properties.

Actually however, it is found that the absolute values of  $\rho_c$  are not directly related to the carrier accumulation variation upon illumination. Indeed, first of all, the variation of the electron and the hole accumulations in the dark with the rise of  $E_a$  is significant: from  $2.91 \times 10^3$  to  $8.86 \times 10^1$  for electrons and from  $3.25 \times 10^{-4}$  to  $1.13 \times 10^{-2}$  for holes, whereas the  $\rho_c$  variation remains relatively small, namely from  $1.06 \times 10^{-2}$  to  $1.63 \times 10^{-2} \Omega \cdot \text{cm}^2$ . Conversely, the electron and the hole accumulations variation with the illumination increase are significantly smaller: from  $2.91 \times 10^3$  to  $8.59 \times 10^2$  for electrons and from  $3.25 \times 10^{-4}$  to  $9.61 \times 10^{-4}$  for holes, however, in that case, the  $\rho_c$  variation is much larger, from  $1.06 \times 10^{-2}$  to  $1.77 \times 10^{-1} \Omega \cdot \text{cm}^2$  (for the case of the shell #4 with  $E_a = 17$  meV). In other words, as prime example, the  $\rho_c$  value at 100% of illumination of the shell #4 featuring an  $E_a$  of 17 meV is higher than the  $\rho_c$  value in the dark of the shell #1 featuring an  $E_a$  of 265 meV, despite a higher electron and lower hole accumulation.

An additional outcome of these results is that considering a  $\Delta N_e$  of about  $2.0 \times 10^{15} \text{ cm}^{-3}$  at MPP [39] and thus a  $R_{sh}$  of about  $50 \Omega/\text{sq}$ , Figure 9c shows that the difference between the  $\rho_c$  value calculated in dark condition (corresponding

to  $R_{sh} \sim 110 \Omega/\text{sq}$ ) and at MPP is between  $0.11$  to  $0.14 \Omega \cdot \text{cm}^2$  for the four different  $E_a$ . Hence, considering that a  $1 \Omega \cdot \text{cm}^2$   $R_S$  induces a FF loss of  $\sim 5\%_{\text{abs}}$  [40], the difference between the induced FF loss calculated at MPP illumination and the one in the dark is between  $0.57\%_{\text{abs}}$  to  $0.70\%_{\text{abs}}$ . It is therefore important to measure the  $\rho_c$  at MPP condition to study accurately the actual impact of a shell on the transport losses and thus on the corresponding effect on FF of solar cells.

Figure 9. (a) and (b) simulated  $R_{sh}$  and  $\rho_c$  as a function of the illumination intensity. (c) simulated  $\rho_c$  as a function of  $R_{sh}$  and (d) slopes from simulated  $\rho_c = f(R_{sh})$ .

## B. TLM under Illumination and non-ohmic Behaviour

### 1) Experimental Evidences

Figure 10a plots the I-V curves experimentally measured for the shell #2, featuring a n-type multilayer with  $E_a$  of 173 meV and high rear side passivation quality, under different illuminations and between two consecutive TLM pads spaced by 2.5 mm. The major observation here is the excellent agreement between the simulations presented in section III.A.1) and the experimental results: The non-ohmic behaviour gets stronger with higher illumination and thus with higher  $\Delta N_e$ . The  $\Delta N_e$  corresponding to the different illumination conditions are given in Table 2. Markedly, the non-ohmic behaviour appears above a certain injected carrier density threshold, here  $2.2 \times 10^{15} \text{ cm}^{-3}$  for an illumination of 50%. In addition, as observed with simulation, the non-ohmic behaviour is present for all the shells under study with the high passivation quality (shells #1 to #4) listed in Table 1. The latter appears at a similar illumination intensity threshold with similar  $\Delta N_e$  values (data not shown), confirming that these shells feature similar passivation quality. Furthermore, the onset of the non-ohmic behaviour is experimentally shown to depend on the passivation quality of the shell under study. This is illustrated in Figure 10b, which plots the TLM I-V curves under illumination of the shell #5, featuring the same n-type multilayer as shell #2 (with namely  $E_a$  of 173 meV) but presenting a low rear side passivation. Although the TLM I-V curves of the shell #2 become non-ohmic with illumination increase, the ones of the shell #5 stay ohmic for all illuminations. This is due to the different passivation qualities and hence to the different injected carrier densities actually reached inside the c-Si(n) bulk for a given illumination. The injected electron density induced by the illumination for both shells is listed in Table 2. Thus, it is experimentally validated that the injected electron density inside the c-Si(n) drives the non-ohmic behaviour of TLM samples, consistently with what was demonstrated by the numerical study presented in section III.A.1).

Figure 10. I-V characteristics as a function of the illumination (in the case of a TLM gap of 2.5 mm) of shells #2 (a) and #5 (b), featuring both the same n-type multilayer with  $E_a = 173$  meV, but with a high and a low rear side passivation quality, respectively.

Table 2. Injected electron density ( $\Delta N_e$ ) as a function of the illumination for the high and low rear side passivation quality of the shell #2 and #5 respectively, featuring both a n-type multilayer with  $E_a = 173$  meV.

Illumination	$\Delta N_e$ ( $\text{cm}^{-3}$ )	$\Delta N_e$ ( $\text{cm}^{-3}$ )
	Shell #2	Shell #5
Dark	0	0
7%	$3.14 \times 10^{14}$	$1.30 \times 10^{14}$
13%	$4.85 \times 10^{14}$	$2.22 \times 10^{14}$
50%	$2.23 \times 10^{15}$	$5.31 \times 10^{14}$
100%	$6.55 \times 10^{15}$	$7.84 \times 10^{14}$

### 2) Simple explanation of the non-ohmicity

Here, the appearance of the non-ohmic regime is demonstrated to be due to a drift of the free carriers induced by the voltage applied between two consecutive TLM pads, leading to a non-homogeneous carrier density and thus a variation of the wafer  $R_{sh}$  below the TLM pads and the gap in-between. Indeed, it is demonstrated by simulation and presented in Figure 11a and Figure 11b (top sketches) that for zero TLM bias ( $\Delta U = 0\text{V}$ ) the generated carriers are homogeneously

distributed inside the bulk (Figure 11a), but as soon as a non-zero TLM bias is applied, here simulated for one volt ( $\Delta U = 1V$ ), a drift of generated-carriers arises, leading to an inhomogeneous carrier density inside the bulk and below both TLM pads (Figure 11b). A simplified case study to illustrate the impact of this effect is presented in Figure 11c and Figure 11d (bottom sketches). Under illumination and at  $\Delta U = 0V$  (no TLM voltage bias), the electrons are homogeneously distributed inside the c-Si(n) bulk along the distance  $L$ , and their density equals  $n_{0e} + \Delta N_e$ , with  $n_{0e}$  the bulk doping density, everywhere within the sample bulk. Under a TLM applied bias  $\Delta U = \alpha V$  (with  $\alpha > 0$ ), the electrons drift because of the applied external field. We now assume these electrons to be distributed following a simple non-homogeneous distribution: in the sample region  $0 < x < L/2$ , the electron density is now  $n_{0e}$ , whereas in the region  $L/2 < x < L$ , the electron density is  $n_{0e} + 2\Delta N_e$ . Note that the total number of electrons (and hence holes) is chosen to be constant inside the whole volume of the sample in both the  $0V$  and the  $\alpha V$  cases. This is equivalent to assuming the same total recombination rate in both cases. Computing now the equivalent resistance of the sample bulk seen by the electrons in the  $0V$  and the  $\alpha V$  cases ( $R_{0V}$  and  $R_{\alpha V}$ , respectively), it turns out that  $R_{0V} < R_{\alpha V}$  (see the Appendix VI.A for the full calculation details). Said differently, the wafer resistance depends on the applied bias  $\Delta U$ , i.e.  $R = R(\Delta U)$ . Hence, the higher the TLM applied bias, the higher the total resistance seen by the TLM current between two TLM pads (as  $R_{\alpha V}$  gets consistently larger values compared to  $R_{0V}$ ). This explains the non-ohmic shape of the I-V curve obtained between two TLM pads measured under illumination. At low voltages however, a linear I-V regime is still present because the drift of charges is small, but as soon as the voltage rises, the non-ohmic I-V behaviour appears, then stabilises at high voltages to a second linear I-V regime. This stabilisation is due to the presence of a maximal drift of carriers, such as the carriers are all completely depleted through the whole silicon bulk. In addition, this second linear regime features a higher slope (i.e. a higher resistance) than the first linear one, evidencing the increase of the c-Si global resistance with the voltage increase (see Figure 10a). Importantly, in any case where the TLM bias induced a non-negligible drift of carriers, two different injection conditions are present below the two TLM pads, which then makes impossible to perform the TLM computation. Thus, to stay in a near-uniform injection throughout the wafer, we chose to perform the TLM computation taking the slope in the first linear regime of the I-V curves (symmetrically around the origin). Illustrative examples of such linear ranges are given in Figure 12 in the case of the shell #2. Note that this drift effect is expected to be present also for other test structures used for  $\rho_c$  characterization such as the one presented in [41]. In that case, the spatial variation in the excess carrier concentration will arise in the vertical direction and will also impact the resulting resistance of the c-Si bulk.

Figure 11. Top: electron density for 1 sun illuminated TLM sample, under 0 (a) and 1 V (b) TLM voltage; Bottom: simplified case study with at 0V (c) the total number of electrons homogeneously distributed inside the c-Si bulk along the distance  $L$ , and at  $\alpha V$  (d), a particular non-homogeneous distribution. This simple case study illustrates that the higher the TLM applied bias, the higher the total resistance seen by the TLM current between two TLM pads ( $R_{0V} < R_{\alpha V}$ ).

Figure 12. I-V curves of shell #2 showing the linear ranges where TLM computation is performed for the case of 100% illumination and for the different gaps. (a) Full I-V range and (b) zoom on the linear range.

### C. TLM Under Illumination and impact on $\rho_c$

Figure 13a-c plot the TLM parameters obtained from our experimental measurements and for the shells #1 to #4 featuring different  $E_a$  (17, 48, 173 and 265 meV, respectively). Figure 13a shows that, consistently with our simulations, the  $R_{sh}$  decreases with rising the illumination for the different  $E_a$ . In addition, it is observed that for the different illuminations the  $R_{sh}$  present similar values for each  $E_a$ , hence revealing similar passivation quality for the different shells under study. The injection conditions corresponding to the different illuminations are listed in

This is the author's peer reviewed, accepted manuscript. However, the online version of record will be different from this version once it has been copyedited and typeset.  
PLEASE CITE THIS ARTICLE AS DOI: 10.1063/1.50042854

Table 3. Figure 13b shows that the  $\rho_c$  drastically increases with the illumination for the investigated  $E_a$ . In particular, it is observed that with the illumination the distribution of  $\rho_c$  for the different  $E_a$  stays the same, but the difference in value of  $\rho_c$  between the different  $E_a$  is more pronounced for higher illumination. Figure 13c plots the  $\rho_c$  as a function of the  $R_{sh}$  experimentally obtained for the four different shells along with the linear  $\rho_c=f(R_{sh})$  fitting curves. Remarkably, our experimental results are consistent with those obtained from numerical simulations (see section III.A.2))<sup>[2]</sup>. Indeed, the  $\rho_c$  value is found to increase linearly with the  $R_{sh}$  decrease and the  $\rho_c=f(R_{sh})$  fitting curves present different slopes for the different shells. The values of the slopes are presented in Figure 13d. Looking at the three  $E_a$  values of 17, 48 and 173 meV, it is observed that the higher the  $E_a$ , the higher the  $\rho_c=f(R_{sh})$  curve slope as predicted by simulation. Generalizing the rationale explained in sections II.A.2) and III.A.2), we can therefore assume that the shell featuring  $E_a$  of 17 meV is the least sensitive to illumination thanks to a high dark electron accumulation and that the shell featuring  $E_a$  of 173 meV presents the highest illumination sensitivity because of a lower dark electron accumulation. From these considerations, it is also important to discuss the drop of the slope for  $E_a$  of 265 meV. This drop suggests that despite a higher  $E_a$ , its illumination impact is smaller than the shell featuring the  $E_a$  of 173 meV. This highlights the fact that, as already well known,  $E_a$  is not the only parameter ruling the accumulation and the illumination response in SHJ solar cells. Other key parameters, especially defect density, are involved and must be considered [18], [19]. In addition, it is observed that the shells with  $E_a$  of 265 and 48 meV feature similar  $\rho_c$  in the dark (0.05 and 0.04  $\Omega\cdot\text{cm}^2$ , resp.) but different slopes of  $2.4\times 10^{-3}$  and  $1.8\times 10^{-3}$   $\text{cm}^2$ , respectively. This result highlights the relevance of our approach: in addition to compare shells based on their resistive losses, it is possible to compare their response to the illumination. A second major observation is that for all  $E_a$  under study, the  $\rho_c$  value obtained under MPP conditions (here for  $\Delta N_e=2.07\times 10^{15}$  and  $R_{sh}$  of 54  $\Omega/\text{sq}$ ) is between 0.07 to 0.17  $\Omega\cdot\text{cm}^2$  higher compared to the one obtained in dark condition. Hence, the difference between the induced FF loss calculated at an illumination corresponding to around MPP and the one in the dark is between 0.35 to 0.85 %<sub>abs</sub> [40]. Thus, to have effective n-type contact stacks a small dark contact resistivity and/or the smallest slope must be targeted so that the contact is as less as possible sensitive to illumination. This again pinpoints the pertinence of our method to assess the quality of the carrier transport under the conditions experienced in the field by solar cells, where injected carriers play an important role.

Figure 13. (a) and (b)  $R_{sh}$  and  $\rho_c$  as a function of the illumination intensity. (c)  $\rho_c$  as a function of the  $R_{sh}$  of different n-type thin silicon layer with activation energy from 17 to 265 meV as well as the linear fits and (d) the corresponding slope as a function of the activation energy.

<sup>[2]</sup> Note that both experimental and simulation data follow the same trend when changing the illumination. However, by comparing the differences between the simulation and the experimental results, it is observed that a much stronger impact of the activation energy on the  $\rho_c$  behaviour is observed experimentally. This may be due to the fact that in the TCAD simulations, perfect hetero-interfaces at c-Si/a-Si:H and n-aSi:H/TCO are assumed. The discrepancies in contact resistivity magnitude between simulations and experiments are then likely suspected to come from the imperfect interfaces which are present in experimental TLM samples.

Table 3. Average experimental values of  $R_{sh}$ ,  $N_e$  and  $\Delta N_e$  of the different shells under study.

<b>Illumination</b>	<b><math>R_{sh}</math> (<math>\Omega/sq</math>)</b>	<b><math>N_e</math> (<math>cm^{-3}</math>)</b>	<b><math>\Delta N_e</math> (<math>cm^{-3}</math>)</b>
<b>Dark</b>	116	$1.64 \times 10^{15}$	0
<b>7%</b>	99	$1.94 \times 10^{15}$	$2.96 \times 10^{14}$
<b>13%</b>	92	$2.09 \times 10^{15}$	$4.55 \times 10^{14}$
<b>50%</b>	54	$3.71 \times 10^{15}$	$2.07 \times 10^{15}$
<b>100%</b>	28	$7.60 \times 10^{15}$	$5.96 \times 10^{15}$

#### ***D. Edges Recombination and its Impact on Contact Resistivity Measurement***

Figure 14a plots the simulated  $R_{sh}(x)$  profiles present below the TLM pad for the different illuminations. These profiles are defined such as the  $R_{sh_{eq}}$ . obtained with equation (3) is matching the values corresponding to the experimental  $R_{sh}$  data for the case of  $E_a = 265$  meV (shell #1) presented in

Table 3. It is observed that  $R_{sh}(x)$  is significantly affected by edge recombination: a strong increase at the TLM pad edges is clearly visible. This is due to a strong decrease of the excess carrier concentration from the middle of the pad to its edges induced by the edge recombination. Then, the contact resistivity profile ( $\rho_c(x)$ ) was calculated considering the experimental dependence between  $\rho_c$  and the illuminated  $R_{sh}$  presented in section III.C. For each  $R_{sh}(x)$  profile, the  $\rho_c(x)$  profile is calculated for the case of  $E_a = 256$  meV using the experimental dependence presented in Figure 13c and is plotted in Figure 14b. Following the experimental evidences of section III.C, it is observed that the higher the  $R_{sh}$ , the lower the  $\rho_c$ . Thus, a significantly smaller value of  $\rho_c$  is observed at the edges compared to the middle of the pad. Then, using equations (4) to (7), TLM computation is performed with the dependence of  $R_{TLMk}$  as a function of the interpad distance of gap  $k$ . The output values of  $\rho_c$  are presented in Table 4 and compared to the experimental ones. It is observed that both experimental and computed values are close: their difference spans from -5.8% to 3.3%. This difference is representative of the global error calculated for all the n-type multilayers under study which were found to be  $\pm 5.8\%$ . This demonstrates that considering the spatial distribution of  $R_{sh}(x)$ , in addition to the experimental linear dependence of  $\rho_c$  with the  $R_{sh}$ , the final values obtained are close to the ones extracted with the standard TLM computation considering a homogeneous  $R_{sh}$ . In addition, note that PC1D simulation neglects the conduction of free carriers inside the thin silicon/TCO stacks which were recently demonstrated to provide efficient lateral transport when combined with the c-Si(n) bulk [42]. If this effect would be relevant for the samples investigated in this paper, it would lead to a homogenisation of the  $R_{sh}$  profile and then mitigate the edge effects. The impact of the non-homogeneous  $R_{sh}$  on the final extracted value of  $\rho_c$  using the standard TLM computation is then limited. Thus, our method to extract  $\rho_c$  under variable illuminations yields a negligible error and is therefore accurate enough to study the  $\rho_c$  evolution as a function of the excess carrier concentration. Note that the TLM pad width could be increased to reduce the error induced by the edge effect. However, doing so, the silver pad conductivity must be adapted to not provide any additional error. Indeed, it has been demonstrated in [38] that the measurement of  $\rho_c$  depends significantly on the TLM pad width for a fixed silver pad conductivity, leading to a rise of the error in the measurement of  $\rho_c$  with the width augmentation.

Figure 14. Equivalent electron sheet resistance profile (a) and contact resistivity profile (b) below the TLM pad width considering the different illumination, for the case of  $E_a = 265$  meV (shell #1).

Table 4. Experimental and computed value of  $\rho_c$  for the case of  $E_a = 265$  meV (shell #1) and for the different illumination intensities.

Illumination	$\rho_c$ ( $\Omega \cdot \text{cm}^2$ )			
	Experimental	Computed	Difference	Error (%)
7%	$1.07 \times 10^{-1}$	$1.01 \times 10^{-1}$	$-6.22 \times 10^{-3}$	-5.8
13%	$1.16 \times 10^{-1}$	$1.16 \times 10^{-1}$	$4.06 \times 10^{-4}$	0.4
50%	$1.96 \times 10^{-1}$	$2.03 \times 10^{-1}$	$6.43 \times 10^{-3}$	3.3
100%	$2.75 \times 10^{-1}$	$2.67 \times 10^{-1}$	$-8.17 \times 10^{-3}$	-3.0

### E. Outlook

As highlighted in the introduction of this paper, solar cells using passivating contact are nowadays reaching high conversion efficiency and approaching their intrinsic efficiency limit. In this quest for maximal efficiency, the higher the device performances, the more difficult it is to identify the way to further improvements. The method presented in this work may insightfully complete already existing ones, such as SunsVoc at very high injection [43] or the works presented in references [9], [26], to further understand and study the electrical transport in solar cells with the aim to guide their actual efficiency improvement. In addition, this method might prove particularly relevant considering the augmentation of the injection level at MPP which goes along with the continuous increase of solar cell efficiencies. Nowadays, record-breaking SHJ devices present MPP injection levels around  $2.9 \times 10^{15} \text{ cm}^{-3}$  [2] and the theoretical

This is the author's peer reviewed, accepted manuscript. However, the online version of record will be different from this version once it has been copyedited and typeset.

PLEASE CITE THIS ARTICLE AS DOI: 10.1063/5.0042854

limit of single junction devices presented by Richter [44] predicts an MPP injection level up to around  $7.9 \times 10^{15} \text{ cm}^{-3}$ . Therefore, the higher the MPP injection, the higher will be the difference between the contact resistivity measured in dark condition and its actual value at MPP for a given shell. This is illustrated in Figure 15 which plots the FF loss difference between different injection conditions and in the dark, considering the linear dependence of the  $\rho_c$  to the  $R_{sh}$  of the shell #3 featuring an  $E_a$  of 48 meV (Figure 13c). The injection considered are those listed in



Table 3. The cases of planar and localized IBC contacts are studied assuming an IBC n-type contact fraction of 40% [4]. The FF loss difference would actually be about 0.9%<sub>abs</sub> considering the theoretical limit of single junction devices as presented by Richter [44], and it would go up to about 1.5%<sub>abs</sub> for the case of Kaneka's record IBC device [2]. This demonstrates that the higher the MPP injection, the less relevant the contact resistivity measured in dark condition would be for an accurate FF losses breakdown. Note that in both cases, the contribution of the c-Si(n) bulk to the final FF loss decreases with the illumination augmentation as its resistivity is reduced. Indeed, a reduction in the FF loss difference between MPP injection and in the dark up to -0.18%<sub>abs</sub> is expected for planar contacts and up to -1.02%<sub>abs</sub> for IBC contact, which will partly counterbalance the augmentation of the FF loss induced by the increase of  $\rho_c$ . Last but not least, it is important to remind that we focused so far on the influence of  $E_a$  only. Yet, it is well known that  $E_a$  is not the only parameter ruling the accumulation and the illumination response in SHJ solar cells. Other key parameters, especially defect density, are involved and must be considered [18], [19]. Overall, our method provides valuable information about the global illumination response of the electron-collecting part of a shell regardless of the individual parameters of each of its sub-components and can then be further generalized to the investigation of other parameters than  $E_a$ . Furthermore, we think our approach to be of general validity and to be equally applicable to investigate shells based on other technologies than SHJ, such as the POLO and the TOPCon ones.

Figure 15. FF loss difference between different injection levels and in the dark, considering the linear dependence of the contact resistivity on the injection of the shell #3 for a planar (grey) and an IBC (blue) contacts. The two dotted lines are guides to the eyes to follow both FF loss evolutions.

#### IV. AVAILABILITY OF DATA

The data that support the findings of this study are available within the article and additionally from the corresponding author upon reasonable request.

#### V. CONCLUSION

In this contribution, we presented a new methodology to characterize the electrical transport quality of SHJ solar cells. First, we introduced the terminology of shell to provide a generalized and unambiguous description of contacts in solar cells allowing to accurately investigate the electrical losses affecting SHJ solar cells. Second, we presented the TLM measurement under variable illumination, which was demonstrated to be a relevant characterization method to investigate and assess the carrier transport quality of n-type SHJ contact stacks. This method revealed a strong dependence of  $\rho_c$  as a function of the c-Si bulk  $R_{sh}$  induced by different injected carrier density. The importance of considering the MPP condition to measure the  $\rho_c$  in order to study the impact on the transport losses and thus on the real value of FF of solar cells is also demonstrated. In addition, this method showed that different n-type contact stacks featuring various  $E_a$  are impacted differently by illumination. These results were supported by TCAD simulation with a particular focus on the  $E_a$  of n-type thin silicon layers to change the accumulation at the c-Si(n)/a-Si:H(i) interface. In addition, the different limitations of this method, namely the non-ohmic behaviour induced by TLM applied voltage and edge recombination were elucidated. Finally, this study presented the first results and investigations of the impact of the illumination on the  $\rho_c$  value and provided the first insights into the involved physical phenomena. However, the global description and understanding of the physical phenomena responsible for the linear rise of  $\rho_c$  with the decrease of  $R_{sh}$ , induced by the illumination increase, are still matters of investigation.

#### VI. ACKNOWLEDGEMENTS

A big and warm thanks to P. Martens for his valuable help and guidance regarding the Python scripts written for this work, E. Wild for her help with the first data treatment, R. Mottet and L. Antognini for their fruitful discussions as well as J. Cattin for providing solar cell sketches. The authors also acknowledge funding provided by the SNSF SHAMAN under Grant Agreement 200021\_192310.

## VII. APPENDIX

A. *Non-ohmic behavior*

In this section the appearance of the non-ohmic regime due to the drift of the free carriers induced by the voltage applied between two consecutive TLM pads is explained in more details. This phenomenon leads to a non-homogeneous carrier density and thus a variation of the wafer  $R_{sh}$  below the TLM pads and the gap in-between. The latter breaks one of the fundamental hypotheses of TLM measurement, which namely states that the  $R_{sh}$  must be homogeneous inside the conductive layer, i.e. inside the c-Si(n) bulk here. Our simple calculations reveal that the higher the voltage bias applied between two TLM pads, the higher the global resistance seen by the TLM current when flowing through the conductive layer (i.e. the c-Si(n) bulk), leading then to a non-ohmic I-V behaviour. Under illumination, free holes and electrons are generated inside the c-Si(n) bulk. First, considering zero applied TLM voltage between two pads, i.e.  $\Delta U = 0V$  voltage bias, the electrons are homogeneously distributed inside the c-Si(n) bulk along the distance  $L$ , and their density equals  $n_{0e} + \Delta N_e$ , with  $n_{0e}$  the bulk doping density, everywhere within the sample bulk (see Figure 11). We then have:

$$R_{sheet_j} = \frac{\rho_j}{d}, \sigma_j = q\mu_j n_j, \rho_j = \frac{1}{q\mu_j n_j} \quad (A.1)$$

with the index  $j$  standing for electron (e) or hole (h),  $d$  the wafer thickness,  $\sigma$  the conductivity,  $\rho$  the resistivity, and  $\mu$  the mobility. These three parameters are then homogeneous inside the wafer and then the resistive contribution  $R$  of the wafer to the total resistance measured between two pads is also homogeneous with:

$$U = RI, I = \frac{U}{R} = U \times \Sigma \quad (A.2)$$

$$\Sigma_j = \frac{1}{R_j} = \frac{\sigma_j}{L} = \frac{q\mu_j n_j}{L} \quad (A.3)$$

With  $U$  the voltage and  $I$  the current between two TLM pads and  $\Sigma$  the conductance (the inverse of  $R$ ).

$$\Sigma_{0V} \propto \frac{n_0 + \Delta n}{L} \quad (A.4)$$

$$\Sigma_{\alpha V} \propto \frac{1}{\frac{L}{n_0} + \frac{L}{n_0 + 2\Delta n}} = \frac{n_0(n_0 + 2\Delta n)}{L(n_0 + \Delta n)} \quad (A.5)$$

And comparing both parameters, we get:

$$\frac{\Sigma_{\alpha V}}{\Sigma_{0V}} = \frac{n_0^2 + 2\Delta n n_0}{n_0^2 + 2\Delta n n_0 + \Delta n^2} < 1 \quad (A.6)$$

$$\frac{R_{0V}}{R_{\alpha V}} = \frac{n_0^2 + 2\Delta n n_0}{n_0^2 + 2\Delta n n_0 + \Delta n^2} < 1 \quad (A.7)$$

Thus, from the computed equivalent resistance of the sample bulk seen by the electrons in the  $0V$  and the  $\alpha V$  cases ( $R_{0V}$  and  $R_{\alpha V}$ , respectively), it turns out that  $R_{0V} < R_{\alpha V}$ . Said differently, the wafer resistance is depending on the applied bias  $U$ , i.e.  $R = R(U)$ . Hence, the higher the TLM applied bias, the higher the total resistance seen by the TLM

current between two TLM pads ( $R_{\alpha V}$  gets larger and larger compared to  $R_{0V}$ ). This explains the non-Ohmic shape of the IV curve obtained between two TLM pads measured under illumination. Therefore, at low voltages, a linear I-V regime is still present because the drift effect is small, but as soon as the voltage increases, the non-ohmic I-V behaviour appears, then stabilises at high voltages to a second linear I-V regime. This second linear regime features a higher slope than the first linear one, evidencing the increase of the c-Si global resistance with the voltage (see Figure 16). In addition, it is also observed that with the increase of the illumination, and thus of  $\Delta N_e$ , the applied voltage required to reach a given current is smaller, i.e. the global resistance is smaller, as the  $R_{sh}$  of the c-Si(n) bulk decreases with  $\Delta N_e$  increase (see Figure 16). Importantly, due to the fact that, for a given TLM bias, both TLM pads feature two different  $R_{sh}$  below them, the  $\rho_c$  is not equal between the two pads, making impossible to perform TLM computation. In addition, the resulting resistance between two TLM pads varies with the TLM bias voltage, but this resistive effect is negligible compared to the wafer  $R_{sh}$  variation with the TLM bias voltage.

Figure 16. I-V characteristics of shells #2 as a function of the illumination, for the TLM gap of 2.5 mm. The injected electron densities are also reported along with the corresponding illuminations.

## REFERENCES

- [1] A. Cuevas, T. Allen, J. Bullock, Y. Wan, D. Yan, and X. Zhang, "Skin care for healthy silicon solar cells," *2015 IEEE 42nd Photovolt. Spec. Conf. PVSC 2015*, no. 1, 2015, doi: 10.1109/PVSC.2015.7356379.
- [2] K. Yoshikawa *et al.*, "Silicon heterojunction solar cell with interdigitated back contacts for a photoconversion efficiency over 26%," *Nat. Energy*, vol. 2, no. 5, 2017, doi: 10.1038/nenergy.2017.32.
- [3] F. Haase *et al.*, "Laser contact openings for local poly-Si-metal contacts enabling 26.1%-efficient POLO-IBC solar cells," *Sol. Energy Mater. Sol. Cells*, vol. 186, no. June, pp. 184–193, 2018, doi: 10.1016/j.solmat.2018.06.020.
- [4] P. Procel, G. Yang, O. Isabella, and M. Zeman, "Theoretical evaluation of contact stack for high efficiency IBC-SHJ solar cells," *Sol. Energy Mater. Sol. Cells*, vol. 186, no. April, pp. 66–77, 2018, doi: 10.1016/j.solmat.2018.06.021.
- [5] U. Würfel, A. Cuevas, and P. Würfel, "Charge carrier separation in solar cells," *IEEE J. Photovoltaics*, vol. 5, no. 1, pp. 461–469, 2015, doi: 10.1109/JPHOTOV.2014.2363550.
- [6] L.-L. Senaud *et al.*, "Aluminium-Doped Zinc Oxide Rear Reflectors for High-Efficiency Silicon Heterojunction Solar Cells," *IEEE J. Photovoltaics*, vol. 9, no. 5, pp. 1217–1224, 2019, doi: 10.1109/JPHOTOV.2019.2926860.
- [7] M. Tanaka *et al.*, "Development of new a-si/c-si heterojunction solar cells: Acj-hit (artificially constructed junction- heterojunction with intrinsic thin-layer)," *Jpn. J. Appl. Phys.*, vol. 31, no. 11 R, pp. 3518–3522, 1992, doi: 10.1143/JJAP.31.3518.
- [8] P. Würfel, *Physics of Solar Cells: From Principles to New Concepts*. 2005.
- [9] A. Fell, J. Schön, M. C. Schubert, and S. W. Glunz, "The concept of skins for silicon solar cell modeling," *Sol. Energy Mater. Sol. Cells*, vol. 173, no. March, pp. 128–133, 2017, doi: 10.1016/j.solmat.2017.05.012.
- [10] E. Yablonovitch, T. Gmitter, R. M. Swanson, and Y. H. Kwark, "A 720 mV open circuit voltage SiOx:c-Si:SiOx double heterostructure solar cell," *Appl. Phys. Lett.*, vol. 47, no. 11, pp. 1211–1213, 1985, doi: 10.1063/1.96331.
- [11] F. Feldmann, M. Bivour, C. Reichel, M. Hermle, and S. W. Glunz, "Passivated rear contacts for high-efficiency n-type Si solar cells providing high interface passivation quality and excellent transport characteristics," *Sol. Energy Mater. Sol. Cells*, vol. 120, no. PART A, pp. 270–274, 2014, doi: 10.1016/j.solmat.2013.09.017.
- [12] U. Römer *et al.*, "Recombination behavior and contact resistance of n+ and p+ poly-crystalline Si/mono-crystalline Si junctions," *Sol. Energy Mater. Sol. Cells*, vol. 131, pp. 85–91, 2014, doi: 10.1016/j.solmat.2014.06.003.
- [13] P. Koswatta, M. Boccard, and Z. Holman, "Carrier-selective contacts in silicon solar cells," *2015 IEEE 42nd Photovolt. Spec. Conf. PVSC 2015*, no. 2, pp. 13–16, 2015, doi: 10.1109/PVSC.2015.7356143.
- [14] A. Richter *et al.*, "Both sides contacted silicon solar cells: option for approaching 26% efficiency," *36th Eur. Photovolt. Sol. Energy Conf. Exhib.*, pp. 90–95, 2019, doi: 10.4229/EUPVSEC20192019-2BP.1.3.
- [15] E. T. Roe, K. E. Egelhofer, and M. C. Lonergan, "Exchange current density model for the contact-determined current-voltage behavior of solar cells," *J. Appl. Phys.*, vol. 125, no. 22, 2019, doi: 10.1063/1.5090519.
- [16] A. Onno, C. Chen, P. Koswatta, M. Boccard, and Z. C. Holman, "Passivation, conductivity, and selectivity in solar cell contacts: Concepts and simulations based on a unified partial-resistances framework," *J. Appl. Phys.*, vol. 126, no. 18, 2019, doi: 10.1063/1.5117201.
- [17] P. Procel *et al.*, "On the Correlation between Contact Resistivity and High Efficiency in (IBC-) SHJ Solar Cells," in *Proceedings of the 36th European Photovoltaic Solar Energy Conference and Exhibition (2019) 2CO.12.6*, 2019, pp. 251–254.
- [18] R. Varache, J. P. Kleider, W. Favre, and L. Korte, "Band bending and determination of band offsets in amorphous/crystalline silicon heterostructures from planar conductance measurements," *J. Appl. Phys.*, vol. 112, no. 12, 2012, doi: 10.1063/1.4769736.
- [19] T. F. Schulze, L. Korte, E. Conrad, M. Schmidt, and B. Rech, "Electrical transport mechanisms in a-Si:H/c-Si heterojunction solar cells," *J. Appl. Phys.*, vol. 107, no. 2, pp. 1–13, 2010, doi: 10.1063/1.3267316.
- [20] M. Jeong, P.-M. Solomon, S. E. Laux, H.-S. P. Wong, and D. Chidambarrao, "Comparison of raised and Schottky source/drain MOSFETs using a novel tunneling contact model," *Int. Electron Devices Meet. 1998 Tech. Dig. (Cat. No.98CH36217)*, pp. 733–736, 1998.
- [21] E. O. Kane, "Theory of tunneling," *J. Appl. Phys.*, vol. 32, pp. 83–91, 1961, doi: https://doi.org/10.1063/1.1735965.
- [22] F. Jiménez-Molinos, F. Gámiz, a. Palma, P. Cartujo, and J. a. López-Villanueva, "Direct and trap-assisted elastic tunneling through ultrathin gate oxides," *J. Appl. Phys.*, vol. 91, no. 8, pp. 5116–5124, 2002, doi: 10.1063/1.1461062.
- [23] D. B. M. Klaassen, "A Unified Mobility Model for Device Simulation - I. Model Equation and Concentration Dependence," *Solid State Electron.*, vol. 35, no. 7, pp. 953–959, 1992.
- [24] D. B. M. Klaassen, "A unified mobility model for device simulation-II. Temperature dependence of carrier mobility and lifetime," *Solid State Electron.*, vol. 35, no. 7, pp. 961–967, 1992, doi: 10.1016/0038-1101(92)90326-8.
- [25] A. Cuevas *et al.*, "Carrier population control and surface passivation in solar cells," *Sol. Energy Mater. Sol. Cells*, vol. 184, no. April, pp. 38–47, 2018, doi: 10.1016/j.solmat.2018.04.026.
- [26] R. Brendel and R. Peibst, "Contact Selectivity and Efficiency in Crystalline Silicon Photovoltaics," *IEEE J. Photovoltaics*, vol. 6, no. 6, pp. 1413–

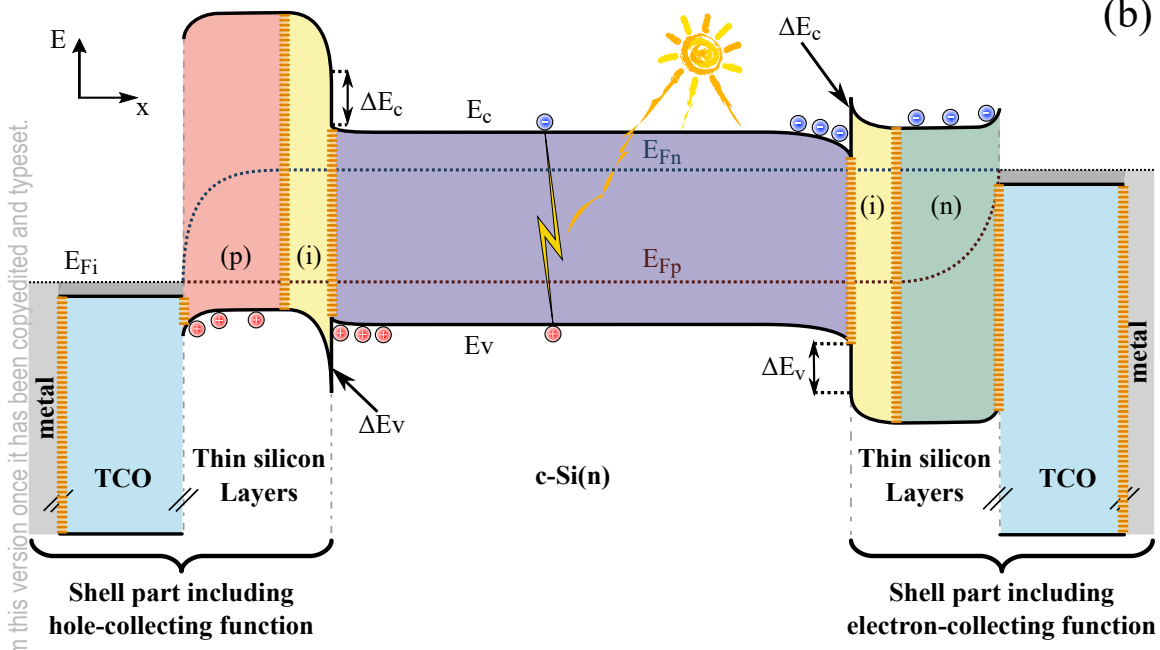
This is the author's peer reviewed, accepted manuscript. However, the online version of record will be different from this version once it has been copyedited and typeset.

PLEASE CITE THIS ARTICLE AS DOI: 10.1063/1.50042854

- 1420, 2016, doi: 10.1109/JPHOTOV.2016.2598267.
- [27] A. Descoeurdes *et al.*, “Improved amorphous/crystalline silicon interface passivation by hydrogen plasma treatment,” *Appl. Phys. Lett.*, vol. 99, no. 12, pp. 2009–2012, 2011, doi: 10.1063/1.3641899.
- [28] A. Descoeurdes *et al.*, “Advanced silicon thin films for high-efficiency silicon heterojunction-based solar cells,” *2017 IEEE 44th Photovolt. Spec. Conf. (PVSC), Washington, DC*, pp. 50–55, 2017, doi: 10.1109/pvsc.2017.8520930.
- [29] L.-L. Senaud *et al.*, “Decoupling bulk and interface properties in the shells of silicon heterojunction solar cells,” *Oral Present. SiliconPV*, 2019.
- [30] L.-L. Senaud *et al.*, “Bottom-up vs Top-down Approaches for Identifying and Mitigating the Transport Losses in High-Efficiency Silicon Heterojunction Solar Cells,” *Oral Present. EUPVSEC*, 2019.
- [31] A. Shah, C. Ballif, W. Beyer, F. Finger, and H. Schade, *Thin-Film Silicon Solar Cells*. EPFL press, 2010.
- [32] D. S. Ginley, H. Hosono, and D. C. Paine, *Handbook of Transparent Conductors*. Springer, Boston, MA, 2011.
- [33] S. Eideloth and R. Brendel, “Analytical theory for extracting specific contact resistances of thick samples from the transmission line method,” *IEEE Electron Device Lett.*, vol. 35, no. 1, pp. 9–11, 2014, doi: 10.1109/LED.2013.2290602.
- [34] Sentaurus, “Sentaurus Device User Guide,” 2015.
- [35] A. Klein *et al.*, “Transparent conducting oxides for photovoltaics: Manipulation of fermi level, work function and energy band alignment,” *Materials (Basel)*, vol. 3, no. 11, pp. 4892–4914, 2010, doi: 10.3390/ma3114892.
- [36] P. Procel *et al.*, “The role of heterointerfaces and subgap energy states on transport mechanisms in silicon heterojunction solar cells,” *Prog. Photovoltaics Res. Appl.*, no. March, pp. 1–11, 2020, doi: 10.1002/pip.3300.
- [37] D. A. Clugston and P. A. Basore, “PC1D version 5: 32-bit solar cell modeling on personal computers,” *Conf. Rec. IEEE Photovolt. Spec. Conf.*, pp. 207–210, 1997, doi: 10.1109/pvsc.1997.654065.
- [38] S. Guo, G. Gregory, A. M. Gabor, W. V. Schoenfeld, and K. O. Davis, “Detailed investigation of TLM contact resistance measurements on crystalline silicon solar cells,” *Sol. Energy*, vol. 151, pp. 163–172, 2017, doi: 10.1016/j.solener.2017.05.015.
- [39] D. Lachenal *et al.*, “Optimization of tunnel-junction IBC solar cells based on a series resistance model,” *Sol. Energy Mater. Sol. Cells*, vol. 200, no. March, p. 110036, 2019, doi: 10.1016/j.solmat.2019.110036.
- [40] D. Pysch, A. Mette, and S. W. Glunz, “A review and comparison of different methods to determine the series resistance of solar cells,” *Sol. Energy Mater. Sol. Cells*, vol. 91, no. 18, pp. 1698–1706, 2007, doi: 10.1016/j.solmat.2007.05.026.
- [41] R. H. Cox and H. Strack, “Ohmic contacts for GaAs devices,” *Solid State Electron.*, vol. 10, no. 12, pp. 1213–1218, 1967, doi: 10.1016/0038-1101(67)90063-9.
- [42] J. Cattin, J. Haschke, C. Ballif, and M. Boccard, “Influence of local surface defects on the minority-carrier lifetime of passivating-contact solar cells. Influence of local surface defects on the minority-carrier lifetime of passivating-contact solar cells,” *Appl. Phys. Lett.*, vol. 113901, no. February, 2020, doi: 10.1063/1.5145351.
- [43] M. Bivour, M. Reusch, F. Feldmann, M. Hermle, and S. Glunz, “Requirements for Carrier Selective Silicon Heterojunctions,” in *Proceedings of the 24th Workshop on Crystalline Silicon Solar Cells & Modules*, 2014, pp. 1–9.
- [44] A. Richter, M. Hermle, and S. W. Glunz, “Reassessment of the limiting efficiency for crystalline silicon solar cells,” *IEEE J. Photovoltaics*, vol. 3, no. 4, pp. 1184–1191, 2013, doi: 10.1109/JPHOTOV.2013.2270351.

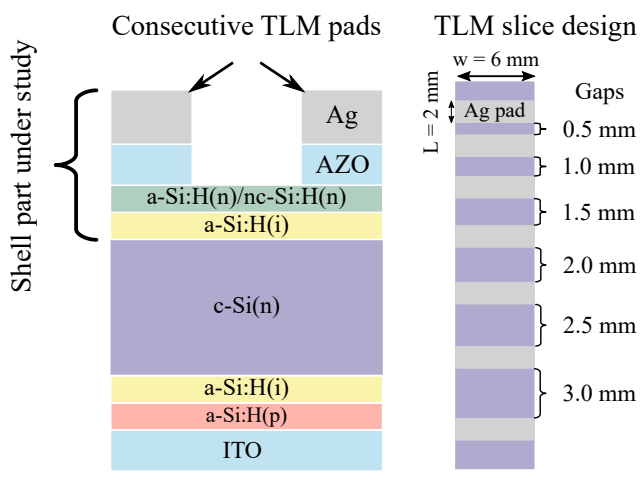
This is the author's peer reviewed, accepted manuscript. However, the online version of record will be different from this version once it has been copyedited and typeset.  
PLEASE CITE THIS ARTICLE AS DOI: 10.1063/5.0042854

This is the author's peer reviewed, accepted manuscript. However, the online version of record will be different from this version once it has been copyedited and typeset.  
 PLEASE CITE THIS ARTICLE AS DOI: 10.1063/5.0042854

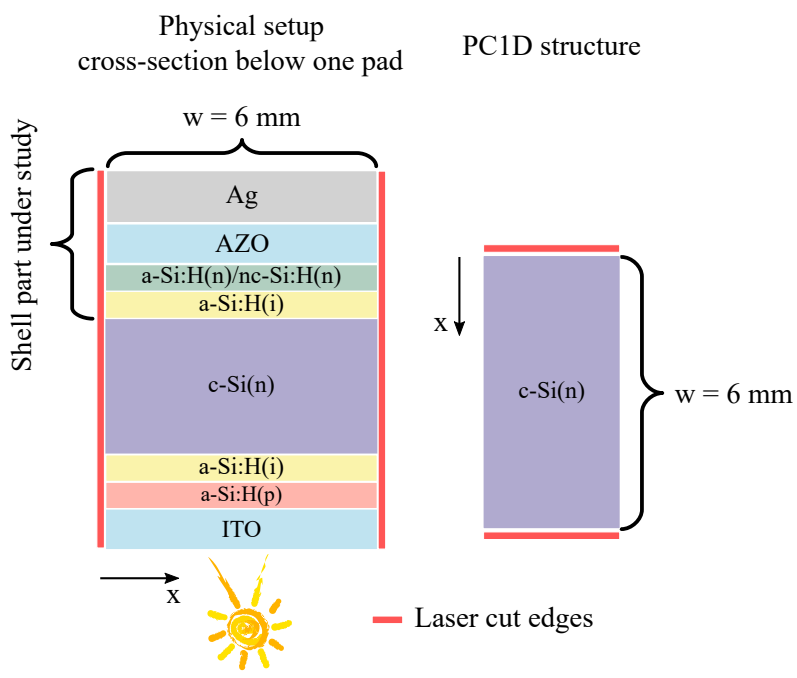


(b)

This is the author's peer reviewed, accepted manuscript. However, the online version of record will be different from this version once it has been copyedited and typeset.  
PLEASE CITE THIS ARTICLE AS DOI: 10.1063/5.0042854

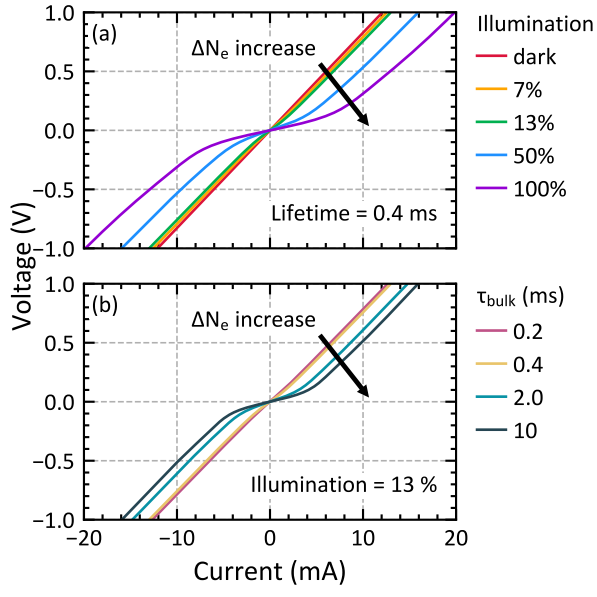


This is the author's peer reviewed, accepted manuscript. However, the online version of record will be different from this version once it has been copyedited and typeset.  
PLEASE CITE THIS ARTICLE AS DOI: 10.1063/5.0042854

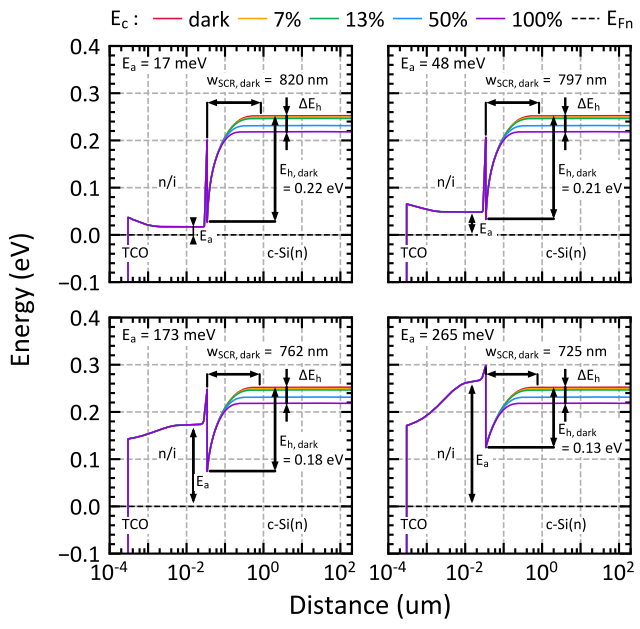




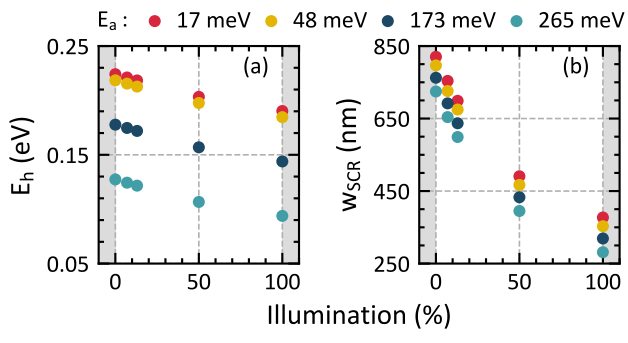
This is the author's peer reviewed, accepted manuscript. However, the online version of record will be different from this version once it has been copyedited and typeset.  
PLEASE CITE THIS ARTICLE AS DOI: 10.1063/5.0042854



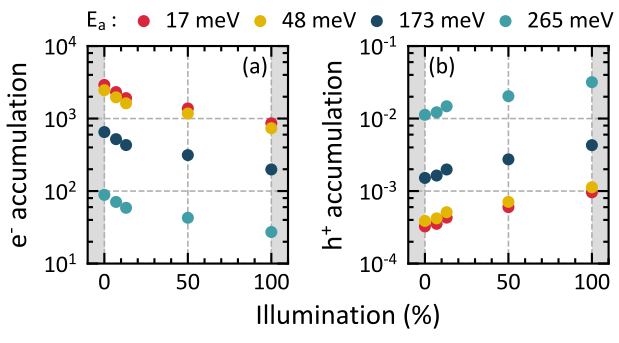
This is the author's peer reviewed, accepted manuscript. However, the online version of record will be different from this version once it has been copyedited and typeset.  
PLEASE CITE THIS ARTICLE AS DOI: 10.1063/5.0042854



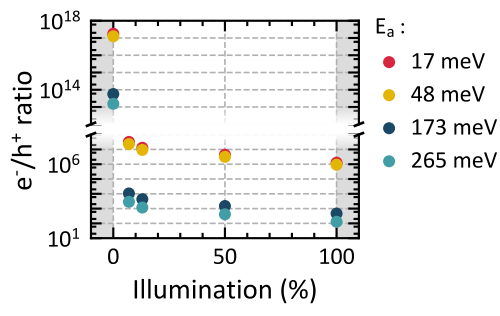
This is the author's peer reviewed, accepted manuscript. However, the online version of record will be different from this version once it has been copyedited and typeset.  
PLEASE CITE THIS ARTICLE AS DOI: 10.1063/5.0042854



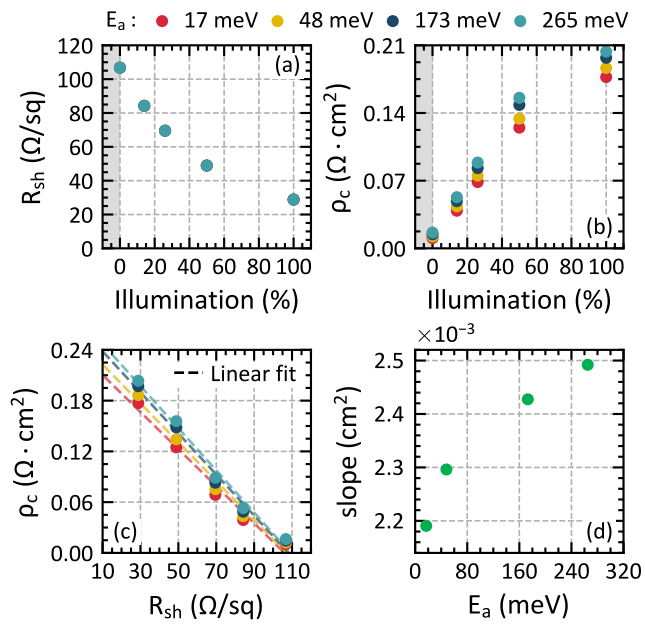
This is the author's peer reviewed, accepted manuscript. However, the online version of record will be different from this version once it has been copyedited and typeset.  
PLEASE CITE THIS ARTICLE AS DOI: 10.1063/5.0042854



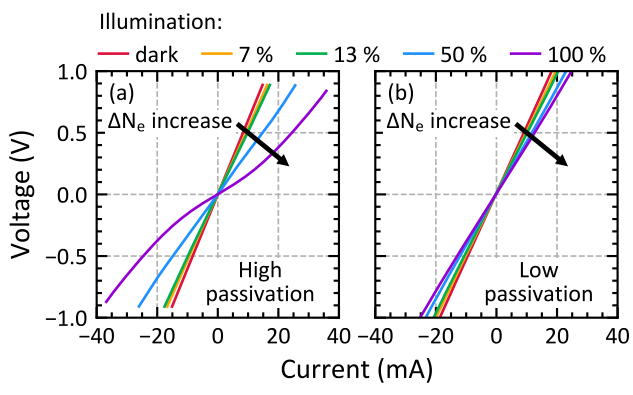
This is the author's peer reviewed, accepted manuscript. However, the online version of record will be different from this version once it has been copyedited and typeset.  
PLEASE CITE THIS ARTICLE AS DOI: 10.1063/5.0042854



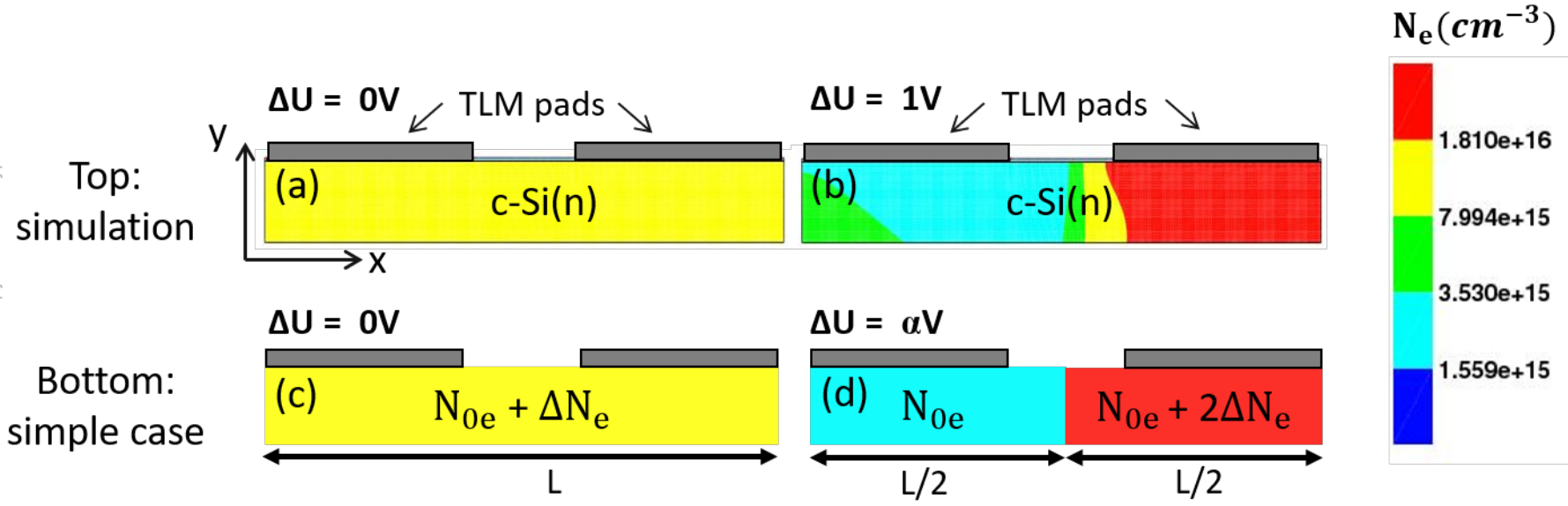
This is the author's peer reviewed, accepted manuscript. However, the online version of record will be different from this version once it has been copyedited and typeset.  
PLEASE CITE THIS ARTICLE AS DOI: 10.1063/5.0042854



This is the author's peer reviewed, accepted manuscript. However, the online version of record will be different from this version once it has been copyedited and typeset.  
PLEASE CITE THIS ARTICLE AS DOI: 10.1063/5.0042854



This is the author's peer reviewed, accepted manuscript. However, the online version of record will be different from this version once it has been copyedited and typeset.  
PLEASE CITE THIS ARTICLE AS DOI: 10.1063/5.0042854



$$\frac{R_{0V}}{R_{\alpha V}} = \frac{N_{0e}^2 + 2\Delta N_e N_{0e}}{N_{0e}^2 + 2\Delta N_e N_{0e} + \Delta N_e^2} < 1$$

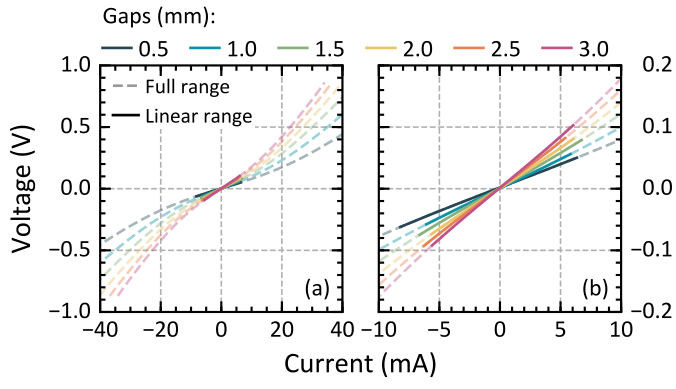
$N_{0e}$ : Dark electron density

$\Delta N_e$ : Injected electron density

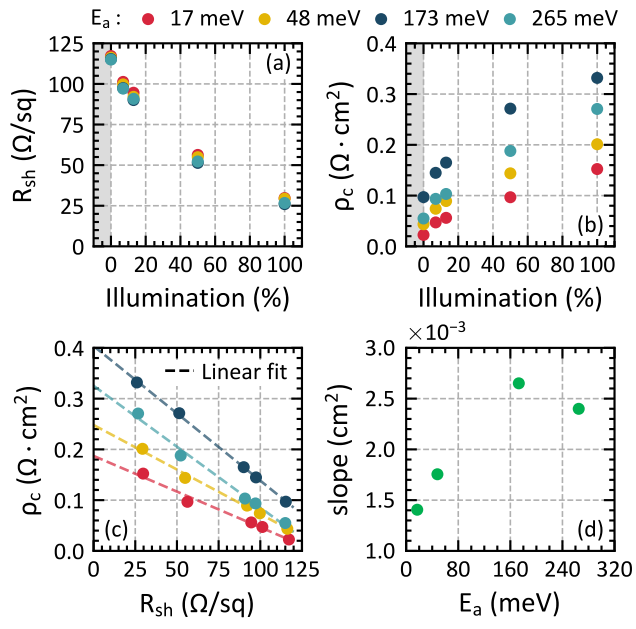
$N_e = N_{0e} + \Delta N_e$ : electron density



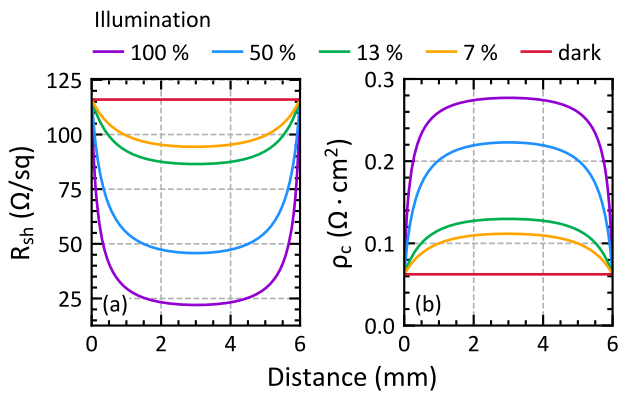
This is the author's peer reviewed, accepted manuscript. However, the online version of record will be different from this version once it has been copyedited and typeset.  
PLEASE CITE THIS ARTICLE AS DOI: 10.1063/5.0042854



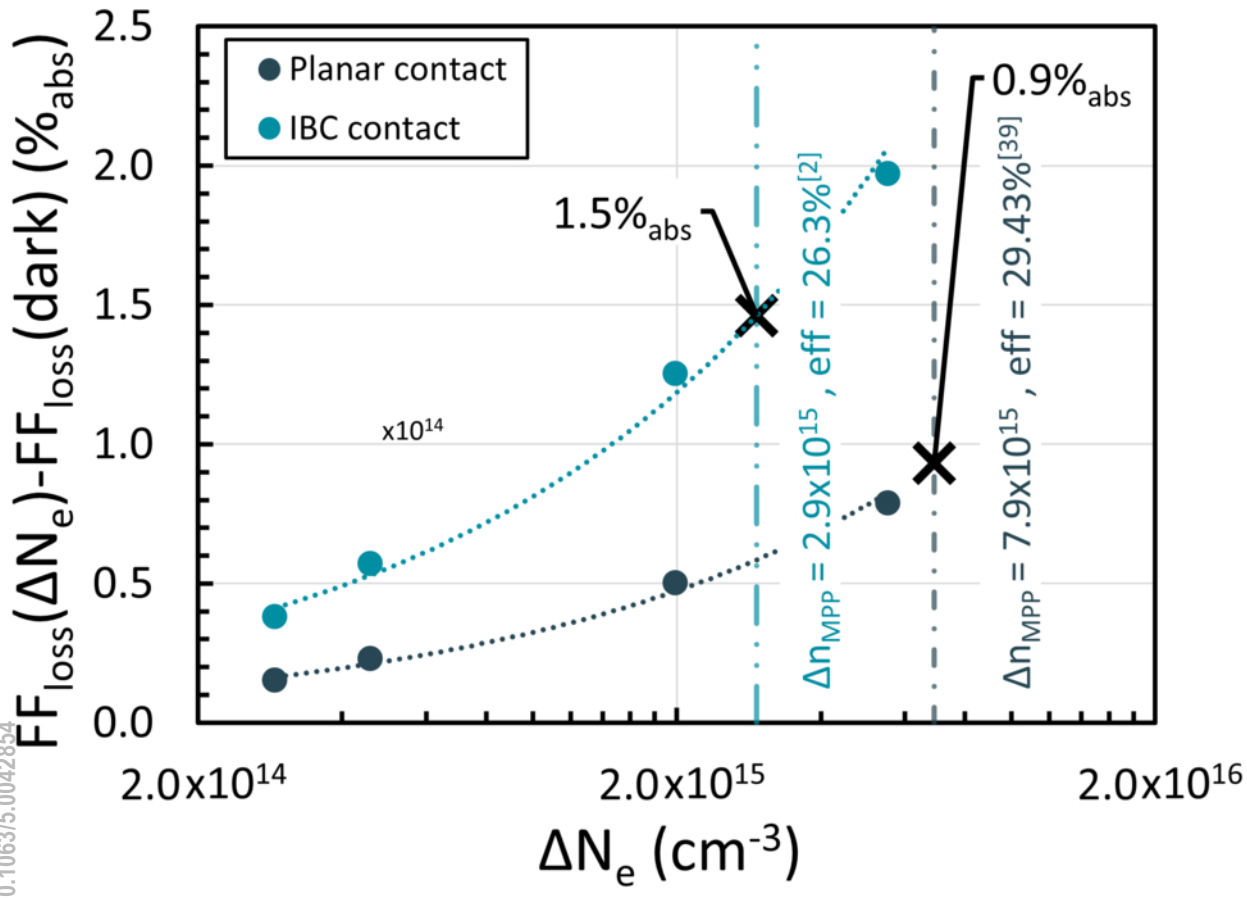
This is the author's peer reviewed, accepted manuscript. However, the online version of record will be different from this version once it has been copyedited and typeset.  
PLEASE CITE THIS ARTICLE AS DOI: 10.1063/5.0042854



This is the author's peer reviewed, accepted manuscript. However, the online version of record will be different from this version once it has been copyedited and typeset.  
PLEASE CITE THIS ARTICLE AS DOI: 10.1063/5.0042854



This is the author's peer reviewed, accepted manuscript. However, the online version of record will be different from this version once it has been copyedited and typeset.  
PLEASE CITE THIS ARTICLE AS DOI: 10.1063/5.0042854



This is the author's peer reviewed, accepted manuscript. However, the online version of record will be different from this version once it has been copyedited and typeset.  
PLEASE CITE THIS ARTICLE AS DOI: 10.1063/5.0042854

